PHYSICAL REVIEW D

PARTICLES AND FIELDS

THIRD SERIES, VOLUME 42, NUMBER 10 15 NOVEMBER 1990

Testing the equivalence principle in the field of the Earth: Particle physics at masses below 1 μeV?

E.G. Adelberger, C.W. Stubbs,* B.R. Heckel, Y. Su, H.E. Swanson, G. Smith, and J.H. Gundlach
Physics Department, University of Washington, Seattle, Washington 98195

W.F. Rogers
Department of Physics and Astronomy, State University of New York at Geneseo, Geneseo, New York 14454
(Received 16 May 1990)

A sensitive, systematic search for feeble, macroscopic forces arising from the exchange of hypothetical ultra-low-mass bosons was made by observing the differential acceleration of two different test body pairs toward two different sources. Our differential accelerometer—a highly symmetric, continuously rotating torsion balance—incorporated several innovations that effectively suppressed systematic errors. All known sources of systematic error were demonstrated to be negligible in comparison to our fluctuating errors which are roughly 7 times larger than the fundamental limit set by the fact that we observe an oscillator at room temperature with a given damping time. Our 1σ limits on the horizontal differential acceleration of Be/Al or Be/Cu test body pairs in the field of the Earth, $\Delta a_\perp = (2.1 \pm 2.1) \times 10^{-11}$ cm s^{-2} and $\Delta a_\perp = (0.8 \pm 1.7) \times 10^{-11}$ cm s^{-2}, respectively, set improved bounds on Yukawa interactions mediated by bosons with masses ranging between $m_b c^2 \approx 3 \times 10^{-18}$ and $m_b c^2 \approx 1 \times 10^{-6}$ eV. For example, our constraints on infinite-range vector interactions with charges of B and of $B-L$ are roughly 10 and 2 times more sensitive than those obtained by Roll, Krotkov, and Dicke using the field of the Sun. Furthermore we set stringent constraints down to λ=1 m, while those of solar experiments are weak for $\lambda < 1$ AU. In terms of the weak equivalence principle in the field of the Earth, our 1σ result corresponds to m_i/m_g(Cu)$-m_i/m_g$(Be)$=(0.2 \pm 1.0) \times 10^{-11}$. Our results also yield stringent constraints on the nonsymmetric gravitation theory of Moffat and on the anomalous acceleration of antimatter in proposed "quantum gravity" models, and have implications for lunar-ranging tests of the strong equivalence principle. Our 1σ limit on the differential acceleration of Be/Al test body pairs toward a 1.5 Mg Pb laboratory source, $\Delta a = (-0.15 \pm 1.31) \times 10^{-10}$ cm s^{-2}, provides constraints on Yukawa interactions with ranges down to 10 cm, and on interactions whose charge is $B - 2L$.

I. INTRODUCTION

One feature common to essentially all extensions of the standard model is the prediction of additional, but so far unobserved, fundamental vector or scalar bosons. For example, why are the apparently conserved vector charges baryon number B, lepton number L, and $B-L$ not the sources of vector fields analagous to the QED and QCD fields generated by the electrical and color charges? Scalar bosons have been proposed to solve many problems, including mass generation (Higgs particles), the smallness of the cosmological constant (dilatons), and the observed clumpiness of the Universe (CP-violating Goldstone bosons). Finally, it has been argued that quantum theories of gravity naturally contain both vector and scalar partners of the conventional tensor graviton.

One ordinarily "explains" the fact that these predicted particles have not been observed by supposing them to be too massive to have been detected in existing experiments. However the possibility that some of these particles have such a low mass ($m_b c^2 < 10^{-6}$eV) that their exchange would generate feeble macroscopic forces has been considered in a variety of contexts,[1-15] several of which would have profound cosmological consequences. In this case, one "explains" the fact that these particles have not been observed by supposing that the forces they

produce are extremely feeble.

The macroscopic potential between unpolarized test bodies, generated by the exchange of ultra-low-mass scalar or vector bosons, has the form

$$V_{12}(r) = \pm\frac{g_5^2}{4\pi}(q_5)_1(q_5)_2\,\frac{e^{-r/\lambda}}{r}\ , \qquad (1)$$

where g_5 is the coupling strength (the + and − signs refer to vector and scalar interactions respectively), $\lambda = \hbar/m_b c$ is the interaction range, and q_5 is the test body charge which is determined by the particular form of the interaction. It is convenient to express this potential as

$$V_{12}(r) = \alpha_5(q_5/\mu)_1(q_5/\mu)_2 G\frac{m_1 m_2}{r}e^{-r/\lambda}\ , \qquad (2)$$

where $\alpha_5 = \pm g_5^2(1/\text{amu})^2/(4\pi G)$ is a dimensionless coupling strength, amu is the atomic mass unit, G is the Newtonian constant, and μ refers to a test body mass in amu.

Macroscopic scalar or vector interactions are distinguishable from the (presumably) much stronger gravitational background because they do not obey the weak equivalence principle, but are composition dependent. This expectation is generic; it follows because the binding energy of matter breaks any exact proportionality between q_5 and mass. Consider a vector interaction with $q_5 = B$. The quantity (B/μ) differs by ≈ 2.5 parts in 10^3 between Be and Cu, two of the test body materials employed in this work. Alternatively, consider a scalar particle coupled to fermion (plus antifermion) number. Strong and electroweak interactions within the test bodies produce virtual fermion-antifermion pairs whose expectation values are a function of the particular material; one therefore expects a composition dependence of the scalar interaction as well. (Although, in principle, a scalar boson could couple to T_μ^μ, higher-order terms apparently always introduce some level of composition dependence.)

The most stringent limits on equivalence-principle-violating macroscopic forces have come from the Roll-Krotkov-Dicke[16] and Braginsky-Panov[17] measurements of the differential acceleration of test bodies toward the *Sun*. These extremely precise limits, however, do not provide strong constraints on interactions of bosons with masses $m_b c^2 > 10^{-17}$ eV because such bosons would produce forces with ranges less than the distance to the Sun.

In this paper we present a full account of our measurements of the differential acceleration of test bodies toward the *Earth*, and towards a massive *laboratory source*. Our results, which have already appeared in Letter format,[18,19] improve existing upper limits on interactions mediated by the exchange of ultra-low-mass bosons by up to two orders of magnitude, and even provide a slightly better test of the equivalence principle than the Roll-Krotkov-Dicke (RKD) experiment. We also set stringent bounds on a proposed nonsymmetric theory of gravity, and on "quantum gravity" models that postulate a pair of macroscopic Yukawa interactions.

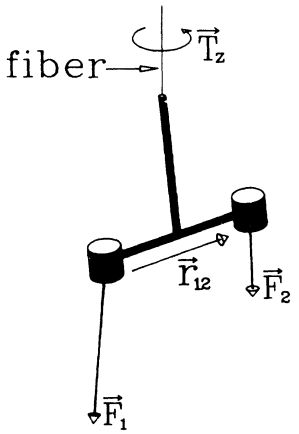

FIG. 1. Operating principle of the torsion balance. This idealized balance consists of two test bodies attached to a rigid, massless frame supported by a torsion fiber. If $\mathbf{F}_1$ and $\mathbf{F}_2$ denote the *net* forces on the two test bodies, the torque about the fiber is given by $T_z = (\mathbf{F}_1 \times \mathbf{F}_2 \cdot \mathbf{r}_{12})/|\mathbf{F}_1 + \mathbf{F}_2|$.

II. APPARATUS

A. General principles

An ideal torsion balance (for simplicity we initially consider a balance containing only two test bodies) experiences a torque about the fiber (vertical) axis if, and only if, as shown in Fig. 1, the net forces on different test bodies do not lie in the same plane. It therefore is a very sensitive instrument for detecting any differences $\Delta\mathbf{a}_\perp$ in the *horizontal* acceleration (force per unit mass) of different test bodies, as could occur if, in addition to gravity and centrifugal forces, a composition-dependent force acted on the bodies (see Fig. 2). The torque due to this differential acceleration is

$$T_5 = \tfrac{1}{2}sm\Delta a_\perp = \tfrac{1}{2}sm\Delta a\sin\delta\ , \qquad (3)$$

where m is the mass of one of the two test bodies, s is the distance between them, and δ is the angle between the average Yukawa force on the test bodies and local vertical (defined by the sum of the gravitational, Yukawa and centrifugal forces). The angle δ plays a large role in determining the sensitivity of torsion balance results to Yukawa interactions of various ranges. For an interaction with $\lambda \gg R_\oplus$ one has

$$\delta \approx \frac{\omega_\oplus^2 R_\oplus \sin 2\Theta}{2g}\ , \qquad (4)$$

where we temporarily assume a spherical Earth of radius $R_\oplus$. Here $\omega_\oplus$ refers to the Earth's rotation frequency, Θ to the latitude of the apparatus, and g to the gravitational acceleration at the Earth's surface. At a latitude $\Theta = 45°$, the angle $\delta \approx 1.7 \times 10^{-3}$. For an interaction with $\lambda \leq R_\oplus$ the situation is more complex. For example, suppose one operated a torsion balance on perfectly

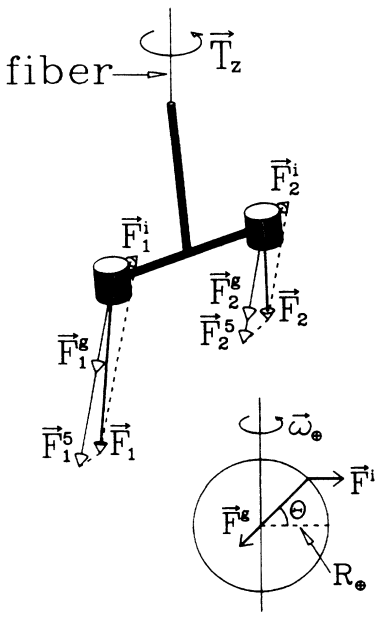

FIG. 2. Forces on a torsion balance located at a latitude Θ. We assume an attractive composition-dependent force F_5 between the test bodies and the Earth that is stronger for body 1 than for body 2. The possible strength of F^5 has been greatly exaggerated and the magnitude of F^g compared to the inertial force F^i has been reduced by a factor of roughly 100.

level terrain (say at sea). One would have no sensitivity to interactions with $\lambda \ll R_\oplus$, because the Yukawa force on a test body would be normal to the Earth's surface, and thus parallel to the torsion fiber. In this case $\delta=0$. On the other hand, a balance operated at the base of a very high ($h \gg \lambda$) vertical cliff "feels" a Yukawa force inclined at 45° corresponding to $\delta=\pi/4$. To obtain good sensitivity for short-range interactions, then, one should place the balance near a topographic feature such as a hill or cliff.

The Yukawa torque on a composition dipole is detected by modulating the relative orientation between the detector dipole and the external source, i.e., by rotating either the apparatus or the source. Heretofore the most precise laboratory torsion balance measurements[16,17] used instruments that were fixed in the laboratory, and a source (the Sun) that rotated smoothly in the laboratory frame. This technique provides an exceptionally smooth rotation and considerable immunity from systematic errors due to ambient magnetic fields and gravity gradients. To overcome the insensitivity of solar experiments to composition-dependent Yukawa interactions with ranges less than 1 AU, we developed a torsion balance that rotates uniformly about the vertical axis ($\omega \equiv 2\pi/\tau_{\rm can}$), and detects differential accelerations towards the Earth or towards laboratory sources. Interactions with ranges down to 10 cm can be probed with our instrument. Although, in principle, we introduce noise into our system by rotating the apparatus, we gain a stronger source (even for an interaction with $\lambda \gg 1$ AU, the horizontal acceleration due to the Earth is ≈ 3 times greater than that due to the Sun), and we place our signal at a considerably higher frequency ($\tau_{\rm can} \approx 2$ h) than the 24 h period of the Sun. This is useful because such experiments are often limited by "$1/f$" noise, and the spectra of other noise sources (such as temperature variations) peak at a 24-h period.

Because we were concerned about possible spurious effects that could arise from irregularities in the turntable drive, we strove for the largest practical angular deflection θ from a given external interaction. The deflection $\theta \propto M/\kappa$ where M is the mass of the pendulum and κ the torsional constant of the fiber. The tensile strength of a fiber is roughly proportional to the square of its diameter d, while κ is roughly proportional to d^4. If one uses the finest fiber capable of supporting the pendulum weight, then the angular deflection from a given external interaction will be inversely proportional to M. We chose 10-g test bodies as a practical compromise between small mass and ease of fabrication.

External torques on the dipole can be detected by measuring either the change in the equilibrium twist in the fiber, or the change in the torsional period, as a function of the angle between the dipole and the external source. We chose to monitor the equilibrium angle because having a complete time history of the dipole (as opposed to knowing only the times when it "crossed through zero") helped us identify and eliminate various unanticipated problems.

B. Symmetry considerations

When searching for a new force that is extremely feeble, subtle effects from the known (and much stronger) interactions can easily produce torques that may masquerade as "new physics." Spurious effects from temperature variations or gradients are particularly insidious because of the large number of mechanisms that could produce effects that mimic a new interaction. Fortunately, most of these mechanisms can be greatly suppressed by incorporating sufficient symmetry into the apparatus. Here we discuss our use of symmetry to minimize possible spurious effects from temperature variations, magnetic and electrostatic forces, turntable drive irregularities, gravity gradients, etc. Because a thorough discussion of systematic errors in solar Eötvös measurements has already been given by Roll, Krotkov, and Dicke,[16] we confine our discussion to issues peculiar to our rotating balance.

1. Symmetries of the test bodies

Dicke[16] has noted that extremely small temperature gradients can generate molecular currents that may apply small torques on the pendulum. We essentially eliminated this effect, and many others as well (electrostatic effects, radiometer effects, etc.), by requiring all test bod-

ies to be "identical on the outside"—i.e., to have the same outside dimensions regardless of their density, and to have the same chemical surface. In addition we obtained good immunity to gravity gradients by designing the test bodies so that their mass quadrupole and octupole moments vanished.

2. Symmetries of the pendulum

Thermal variations can also affect the system that monitors the very small angular deflection of the pendulum. This can occur via thermal expansion of mechanical elements in the optics, or from the temperature sensitivity of semiconductor electronics. We therefore designed the apparatus so that we could precisely reverse the orientation of the composition dipole with respect to *everything else* in the apparatus (including the fiber and the entire optical readout system). By always taking data divided equally between both orientations of the dipole with respect to the remainder of the apparatus, we canceled essentially *all* effects that were not associated solely with the orientation of the composition dipole with respect to the external source. In particular, this reversal of the dipole essentially eliminates any time-independent effects associated with (1) the orientation of the angular deflection monitor in the laboratory such as could occur from ambient temperature gradients, etc., (2) coherent irregularities in the turntable drive caused by imperfections in the bearings or in the gear train, or (3) any magnetic or gravitational effect associated with parts of our system other than the test bodies themselves. Of course, any systematic error that varies in time will not be exactly canceled by reversing the composition dipole. However, we were able to place tight limits on the time stability of our apparatus by comparing data taken with a given composition dipole configuration at widely spaced time intervals.

Gradients in the gravitational field can generate nonparallel forces on test bodies that may masquerade as a new interaction. These gradients are more troublesome with a terrestrial source than with a solar source, because the source is so much closer. We minimized spurious effects from gravity gradients by employing four test bodies, two of one material and two of another. The composition-dependent interaction sees the pendulum as a dipole and produces a torque that varies with ϕ, the angle between the dipole and the external source as $\tau_5 \propto \sin\phi$. We refer to this as a 1ω signal.

The gravitational torque on a pendulum at an angle ϕ with respect to a fixed source is conveniently expressed in the multipole formalism:

$$T_{\rm grav}(\phi) = \kappa\bar{\theta}(\phi) = -4\pi i G \sum_{l=0}^{\infty} \frac{1}{2l+1} \sum_{m=-l}^{+l} m\bar{q}_{lm} Q_{lm} e^{-im\phi} , \tag{5}$$

where

$$\bar{q}_{lm} = \int \rho_{\rm det}(\mathbf{r}) r^l Y^*_{lm}(\hat{\mathbf{r}}) d^3r \tag{6}$$

is evaluated in the body-fixed frame centered on the pendulum c.m., and

$$Q_{lm} = \int \rho_{\rm source}(\mathbf{r}) r^{-(l+1)} Y_{lm}(\hat{\mathbf{r}}) d^3r \tag{7}$$

is evaluated in the laboratory. The $m = 0$ moments produce no torques and can be neglected. The $m = \pm 1$ components are particularly important because they mimic the signal from a new interaction. Because the c.m. must hang directly under the fiber support, $\bar{q}_{11}$ vanishes and the lowest order 1ω gravitational torque arises from the Q_{21} gradient.

We employ four equal mass test bodies (each having vanishing mass quadrupole and octupole moments) on a pendulum tray having four-fold axial symmetry. For an ideal tray and test bodies, all $\bar{q}_{lm}$ with $m < 4$ would vanish. The leading-order signal from gravitation is then small, being due to the fourth derivative of the gravitational potential, and occurs at 4ω. Furthermore, by a simple interchange of the four test bodies, we can configure the pendulum either as a composition dipole or as a composition quadrupole. This provides a useful check on possible systematic errors.

Finally, our design made the $\bar{q}_{20}$ moment of the entire pendulum vanish. (The $\bar{q}_{30}$ moment was small because the pendulum had approximate reflection symmetry about a horizontal plane passing through the c.m.) This feature renders us relatively immune to small misalignments of the fiber attachment point which could otherwise rotate $\bar{q}_{20}$ to produce a troublesome $\bar{q}_{21}$ moment.

3. Symmetries of the apparatus as a whole

Insofar as possible, the apparatus had cylindrical symmetry about the vertical axis, and items which unavoidably broke the symmetry (such as the turntable drive motor) were placed as far from the apparatus as practical. For example, the apparatus rotated inside a cylindrically symmetric Cu shield that was held at a constant temperature. Largely because of these symmetries in our apparatus, we were able to demonstrate that all known systematic errors essentially canceled and were negligible compared to our fluctuating errors.

C. The Eöt-Wash instrument

1. Overview

A schematic scale elevation view of our instrument is shown in Fig. 3. The instrument was placed in a small, sealed, ground floor room in the University of Washington Nuclear Physics Laboratory (latitude $\Theta = 47.66°$). The electronics and data-acquisition computer were located in an adjacent room. The laboratory is built on a hillside in the northeastern corner of the University cam-

pus, approximately 26 m above Lake Washington. The small room abuts the uphill excavation for the laboratory; thus the hillside provides a reasonable source for Yukawa interactions with ranges down to a few meters. The source strength for short range interactions was augmented by adding a layer of cement blocks against the uphill (east-facing) wall of the small room. We preferred to forgo the greater source strength we could obtain at a remote site (a mountain cliff, for example) to have the advantages of a laboratory environment.

2. *Pendulum and test bodies*

The pendulum was designed using a computer program that calculated from a given mass distribution the $\overline{q}_{20}$, $\overline{q}_{21}$, and $\overline{q}_{30}$ moments, the overall moment of inertia, and the location of the system center of mass. Spurious moments arising from finite machining and positioning tolerances could be modeled and analyzed as well.

An assembly view of the pendulum is shown in Fig. 4. The pendulum consists of a thin circular aluminum tray that holds the two pairs of test bodies in shallow recesses, and also supports four 90° mirrors used to monitor the pendulum's angular deflection. (The four mirrors allow the pendulum to hang at any of four angles inside the can.) The pendulum also contains two counterweights mounted above and below the tray on the ends of a vertical axle. Their masses and positions were chosen to satisfy two constraints: the quadrupole moment $\overline{q}_{20}$ of the entire pendulum (including test bodies, mirrors, axle, and the small fiber mounting screw) should vanish, and the c.m. of the pendulum should not change (to within 0.02 mm) if the test bodies are removed.

The pendulum tray, vertical axle, and the top and bottom balance pieces were machined from 7075 Al. The four recesses which position the test bodies are coplanar within ± 13 μm, and constrain the test bodies to sit at radial distance 27.56 ± 0.01 mm from the fiber axis. The vertical axle of the pendulum was polished to a diameter slightly exceeding a gauge fit to the 3.18-mm-diameter central hole in the tray. It was then gently pressed into place and secured by a drop of Loctite glue. Its orthogonal alignment to the tray was adjusted on a lathe until the tray run out was approximately 0.01 mm. The 90° mirrors were fabricated by sawing apart commercial glass cuvettes.[20] Each mirror was glued into place using a jig which precisely constrained the angle and horizontal position. The entire pendulum was covered with an evaporated layer of Au with a thin undercoating of Al (except for the mirrors which had only Au).

Six cylindrical test bodies were fabricated, two each from high-purity beryllium, high-purity aluminum, and oxygen-free high-conductivity (OFHC) copper. All had nominally identical masses and outside dimensions ($h = 17.341 \pm 0.008$ mm, $d = 19.977 \pm 0.008$ mm), and had vanishing mass quadrupole moments ($\overline{q}_{20} = 0.000 \pm 0.005$ g cm^2). To accommodate the different densities, the beryllium bodies were solid cylinders, and the aluminum and copper bodies were hollow cylinders fitted with end caps. The end caps were fabricated approximately 8 μm over diameter and were mounted into the cylindrical bodies by a cold (liquid-nitrogen temperature) press fit. The Be bodies were given small 3.18 mm deep holes in the

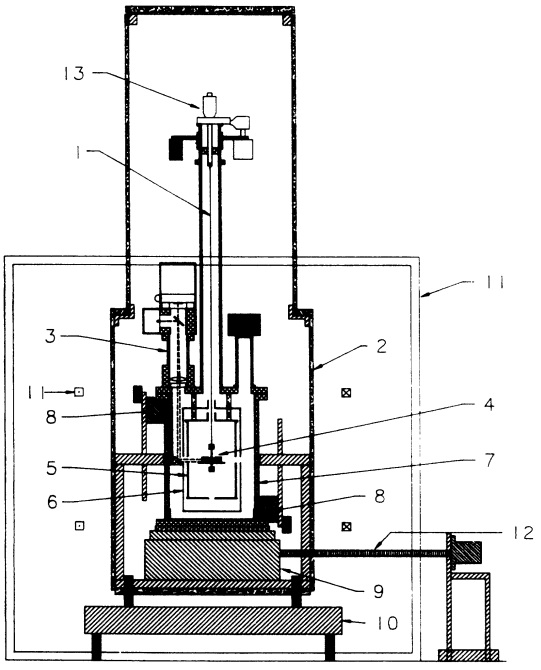

FIG. 3. Schematic side view of the differential accelerometer. The major components are labeled (1) W fiber, (2) thermal shield, (3) autocollimator, (4) torsion pendulum, (5,6) magnetic shields, (7) vacuum vessel and outermost magnetic shield, (8) gravity gradient compensator, (9) turntable, (10) baseplate vibration isolator, (11) Helmholtz coils, (12) turntable drive shaft, (13) fiber positioner. The scale drawing is to scale; the square Helmholtz coils have a side length of 123 cm.

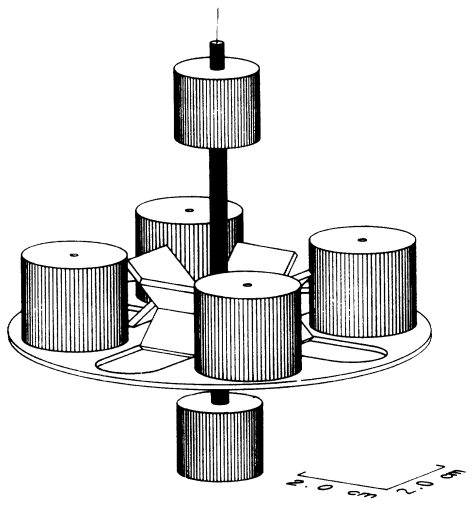

FIG. 4. Scale drawing of the torsion pendulum.

center of the top and bottom surfaces to mimic the identically sized pumpout holes of the Al and Cu bodies.

The test body masses were precisely trimmed by sanding and polishing the pieces both before and after assembly. The mean and standard deviation of the resulting buoyancy-compensated masses of the six uncoated test bodies was (10.03178 ± 0.00020) g. After evaporating a thin Al undercoat and an outer Au film over all outside surfaces, the test body masses increased by (0.00577 ± 0.00014) g.

The axial position of individual test body c.m.'s coincided with their geometrical centers to within 7.6 μm. The c.m.'s were located using a small rigid-beam balance whose pivot was a 3.18-mm-diameter steel dowel pin on a glass slide. The angle of the balance beam was monitored by reflecting a laser beam from a mirror mounted on the balance onto a vertical scale $\approx$2.5 m from the balance. One of the six test bodies was placed in a precisely machined slot on the balance with its cylindrical axis horizontal and orthogonal to the pivot axis of the balance. The beam balance was then leveled by adjusting a counterweight on the other end of the beam to bring the laser beam spot to a mark on a distant wall. The test body was then removed from the balance, rotated end for end, put back in the balance, and the laser spot brought back to its original centered position by moving small calibration masses along the beam. The position of these calibration masses determined the axial location of the test body c.m. relative to its geometrical center. Each of the other five test bodies was then separately placed on the balance in the same slot, and the balance releveled. This determined the c.m. of the remaining test bodies relative to that of the first.

Our design of the test bodies and the pendulum ensured (ignoring roundoff errors and machining tolerances) that the first mass multipole moment of the loaded pendulum that could mimic a true signal nominally occurs in the l=5 multipole order. The reader may notice that we concentrated on making the static properties of the test bodies (i.e., their multipole moments) identical. We could not simultaneously make their dynamic properties (i.e., their moments of inertia) identical as well. However, the moments of inertia of the Cu and Be test bodies about the pendulum c.m. differed by only 3.3%. This difference was insignificant because in our measurements the pendulum was essentially static.

3. Torsion fiber

All data were taken with the same fiber—a 20-μm-diameter 80-cm-long Au-coated W wire.[21] The fiber was soldered to fittings at each end. The bottom fitting (a 3-56 screw) was directly threaded into the torsion pendulum. The top of the fiber was joined to a similar 75-μm-diameter, 2.5-cm-long fiber by a 63-mg Cu sleeve. This thicker fiber was soldered to a Cu cap that screwed onto a Cu rod. The rod penetrated an O-ring vacuum seal and attached to a commercial micrometer and rotation stage[22] that produced controlled vertical and rotary motion. The compound fiber minimized "tilt feedthrough" (discussed in Sec. IV D 2 below) caused by small asymmetries in the fiber at the top attachment point. We observed that these asymmetries are a greater problem in fine fibers than in thick ones. In our design the attachment of the fine fiber is always vertical, regardless of the turntable tilt.

Our pendulum loaded the fiber to $\approx$ 70% of its breaking strength. (Plastic deformation did not begin until the tension exceeded $\approx$ 95% of the breaking strength.) We observed that the fiber "unwound" with a reproduceable pattern each time after it was placed under tension, but that the drift settled down in a few days to $\approx$1.5 μrad/h.

4. Shielding

It was essential to shield the pendulum from all external influences other than those for which we searched. Here we discuss shielding of atmospheric, magnetic, electrostatic, thermal, and gravitational effects.

The pendulum was placed in the center of a massive Al vacuum can (radius=12.9 cm and height=38 cm) that was pumped out to about 2 mTorr before the beginning of each data taking cycle. During the course of data taking, the pressure would rise linearly at a rate of $\approx$2 mTorr/h. As shown in Fig. 5, the viscous damping of the pendulum in this residual gas ($Q \equiv \pi\tau_{\text{decay}}/\tau_{\text{torsion}}$, where τ_{decay} and τ_{torsion} are the exponential decay constant and the free oscillation period of torsional amplitude oscillations respectively) was effectively independent of pressure ($Q \approx 17$) for pressures at which data was taken. This damping was not a limiting factor, and in fact was beneficial because it reduced the amplitude of torsional oscillations pumped by imperfections in the turntable drive.

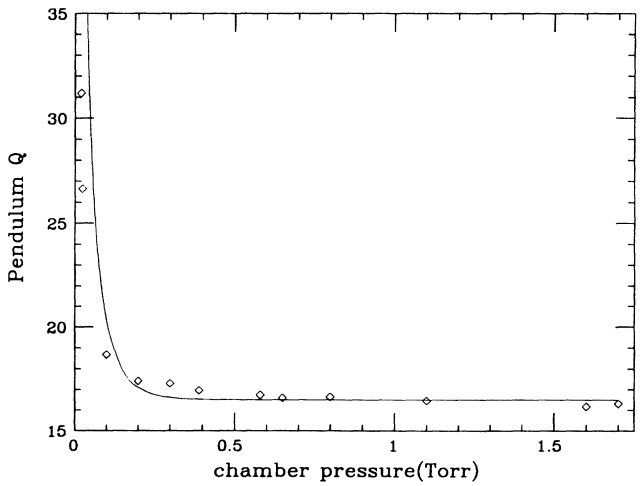

FIG. 5. Pendulum Q as a function of residual gas pressure in the vacuum chamber. Before each equivalence principle data taking cycle, the chamber was evacuated. Data taking did not begin until the pressure had risen to $\approx$ 0.1 Torr.

External magnetic fields were canceled by a three-axis set of Helmholtz coils; vertical fields by circular coils with a diameter of ≈80 cm, horizontal fields by square coils with a side length of ≈121 cm and separated by ≈66 cm. The pendulum itself was surrounded by three concentric annealed mu-metal[23] magnetic shields that rotated with the apparatus. The innermost shield, ≈2 cm from the test bodies, was plated with Au to provide electrostatic shielding as well. The two inner shields, located inside the vacuum can, had tight-fitting lids, and were supported by four rods, three of which were insulating and one was conducting. This minimized any galvanic currents and thermal gradients in the inner shields. The third shield, without lids, fit snugly around the outside of the vacuum can. To further reduce any magnetic perturbations from the turntable bearing and drive, an annealed mu-metal disk was placed inside the bottom of the vacuum can.

The attenuation factors of our magnetic shields were determined by removing the shields, placing a three-axis flux-gate magnetometer at the position of the pendulum and canceling the ambient field to $\leq$ 1.0 mG with the Helmholz coils. By turning the Helmholz coil currents on and off with various shields back in place, we determined that the outermost shield attenuated magnetic field changes in the horizontal plane by a factor of 25, and that the shielding factor of the two inner shields together was $\geq$ 2800 in the horizontal plane and $\approx$ 2000 in the vertical direction (see also Sec. IV D 4).

Thermal shielding was provided by the magnetic shields and by the massive Al vacuum can. Additional thermal shielding was provided by enclosing the entire rotating portion of the instrument inside an azimuthally symmetric, hermetic thermal shield. This shield consisted of 1.6-mm-thick Cu plates in good contact with Cu tubing through which we circulated water from a constant-temperature bath.[24] The outer surface of the shield was covered by 19 mm of plastic foam insulation followed by a layer of aluminized mylar.

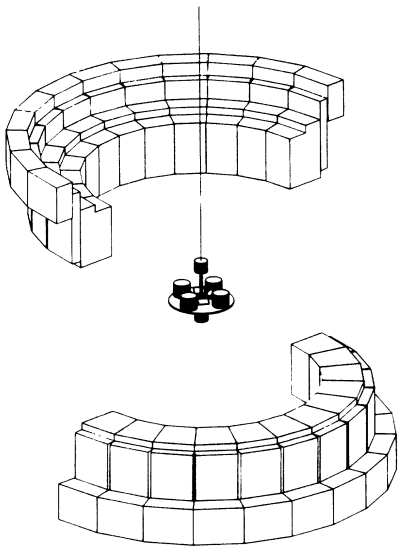

FIG. 6. Gravity gradient compensator. This distribution of mass was used to generate a Q_{21} gravitational field at the pendulum c.m., having a magnitude equal to that of the ambient Q_{21} gradient in the laboratory. An azimuthally symmetric support system is not shown.

Any Q_{l1} gravity gradients can produce 1ω torques on the pendulum that mimic "new physics" if the pendulum has corresponding $\overline{q}_{l1}$ imperfections. A Q_{21} gradient will be present at a hillside unless the apparatus is exactly at the effective midpoint of the hill. Calculations of the gradients at our site showed that the predominant effect was due to the excavation of our laboratory. Because the apparatus was relatively far from the exterior wall ($s/2R \approx 0.01$, where R=1.7 m is the distance from the instrument to the wall), the largest gradient came from the Q_{21} field, and Q_{l1} fields with $l > 2$ were negligible. We therefore placed inside the thermal shield a gradient "compensator"—a rotatable mass distribution shown in Fig. 6 that generated a Q_{21} field which normally cancelled the ambient gradient. The symmetry of the compensator ensured that Q_{l1}=0 for all odd l, Q_{lm}=0 for $2 \leq m \leq 24$, and that Q_{41} vanished by design.

5. *Turntable*

Our terrestrial source data were taken using a turntable based on a commercial single-axis goniometer[25] constructed primarily from Al. The ball bearings did contain ferromagnetic components, but these were degaussed before use. The turntable was driven through 7200:1 reduction gearing by a stepper motor having 10 000 steps/turn. The motor was water cooled and connected to the turntable reduction gears by a wooden shaft that provided thermal and vibration isolation. The motor was powered by a computer controlled oscillator. This circuit divided the output of a stable crystal clock by programmable integral values, allowing us to hold τ_{can} constant at closely spaced values.

The turntable was attached to a massive Al baseplate and Pb vibration dampers by three leveling screws, two of which were driven by stepper motors for remote leveling of the turntable axis. The baseplate was supported above the floor by three Pb blocks to provide some isolation from seismic noise.

We avoided any unnecessary forces on the instrument by routing the signal and electrical power cables from the rotating apparatus through a "corotator" before they went to the stationary electronics. The corotator was attached to the outer thermal shield and contained a motor-driven sleeve nominally coaxial with the rotation axis of the turntable. An optical sensor controlled the sleeve rotation so that it always tracked the turntable. In this way any forces required to twist the cables were provided by the corotator and not by the turntable itself.

6. *Angular deflection readout*

The angular deflection of the pendulum was measured using an autocollimator that was insensitive to plane

pendulum motion of the torsion pendulum, but gave a large signal for torsional motion. Red light from a light-emitting diode[26] (LED), square-wave modulated at 182 Hz with an optical power output of 0.15 mW, was fed via an optical fiber to the focal point of a lens with a focal length f=21.7 cm (f was measured by finding the focus of a parallel light beam on an optical bench). The resulting parallel beam passed through a window into the vacuum system, where it was directed onto the pendulum by a 45° mirror. Essentially all of this light was retroreflected from the pendulum by a corner mirror having a 90° opening angle, and eventually brought to focus on a position-sensitive photodetector[27] mounted on a translation stage. The detector current corresponded to $\approx 6 \times 10^{10}$ photons/s.

The currents from the two ends of the photodetector were converted with low-noise electronics into ac coupled *sum* and *difference* signals. These signals were then demodulated by lock-in amplifiers (time-constants typically 30 s) referenced to the LED drive, and digitized by ±4096 bit analog-to-digital converters (ADC's). The angular deflection θ was obtained by dividing the *difference* ADC value by the *sum*.

The autocollimator performance was not limited by photon statistics, but by fluctuating currents from one end of the photodetector to the other ($R \approx 5$ kΩ) driven by offset voltages in the input stages of the current-to-voltage converters. The photocurrents were large enough that the uncertainty in θ from the fluctuating offsets was $\approx$ 10 times smaller than the observed 1ω noise and did not limit the precision of our results.

7. Other monitors

The can angle ϕ was measured using a shaft encoder with a resolution of 900 000 pulses/revolution.

The turntable tilt was measured using two independent systems: a commercial two-axis electrolytic tilt sensor[28] mounted on the can lid, and an optical system that focused crossed LED beams on the fiber and imaged the diffraction patterns on split photodiodes. We assumed that the can was rotating about the vertical axis when the 1ω component of all tilt signals vanished. The optical fiber monitors also were used to detect any plane pendulum motion of the torsion balance.

Spatial and temporal temperature variations were monitored by seven commercial temperature sensors.[29] Two of these were placed on opposite sides of the vacuum can lid, and one each on the turntable baseplate, the heat shield midpoint, and the water reservoir of the temperature controller. Two other sensors measured the temperature of the air in the small room and the air inside the hermetic heat shield.

8. Data acquisition

At equally spaced time intervals (typically 20 s), all sensors (the two autocollimator signals, shaft encoder output, two tilt monitor signals, two fiber monitor signals, and seven temperature monitor outputs) were recorded by an IBM PC/AT computer, displayed as a function of time, and eventually stored on diskettes for off-line analysis. The computer was also used to control the turntable speed and direction, the leveling adjustments, and the angle of the top fiber attachment.

III. DATA ANALYSIS

A. Signal extraction

A typical sample of our raw angular deflection data is shown in Fig. 7 where we display the output of the *difference* lock-in as a function of time. The raw *difference* signal was first scanned for "fiber quakes" (an example is shown in Fig. 8) and rejected if a visible quake was present. (Fiber quakes were infrequent and were often correlated with seismic disturbances.)

The free torsional oscillations of the pendulum (τ_{torsion}=718 s) are readily apparent in Fig. 7. These oscillations are pumped by small coherent irregularities in the can rotation drive, and by smaller stochastic perturbations. As we were not interested in these free oscillations, but rather in the quasiequilibrium angle of the pendulum, we averaged the readings of all sensors over one complete torsional period (in this process converting from ADC bits to physical units). Figure 9, showing a plot of θ as a function of ϕ, is a typical result of the averaging procedure. (Replacing this procedure by a sixth order Butterworth digital filter gave essentially the same results as simple averaging.)

We extracted our signal from this averaged data by Fourier analysis. Any interaction of our composition dipole with the uniform component of the field from an external source would produce a 1ω torque on the pendulum. On the other hand, gravitational interactions of our pendulum with external masses produced a weak 4ω

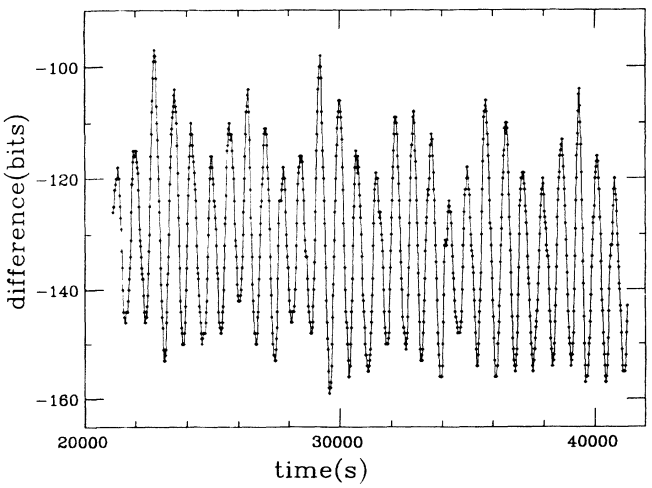

FIG. 7. Typical raw angular displacement data showing the *difference* signal as a function of time.

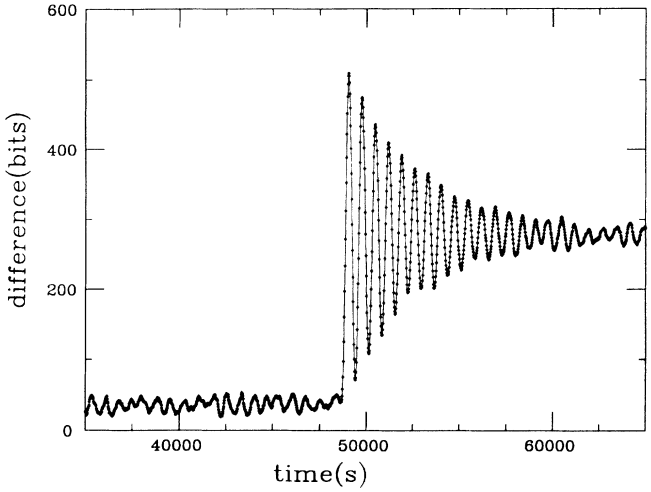

FIG. 8. A typical "fiber quake"in which the fiber suddenly changes its equilibrium angle. The raw *difference* signal is plotted as a function of time. One bit on the vertical axis corresponds to roughly 0.9 μrad. The amplitude decays with a time constant of $\approx$ 3800 s.

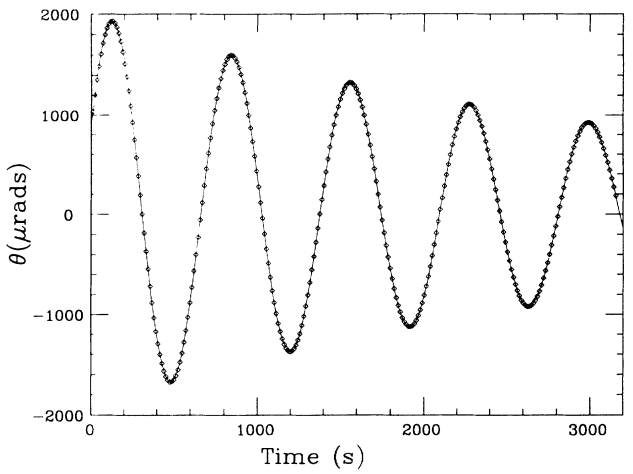

FIG. 10. Dynamic calibration, showing the pendulum response to an abrupt change in the turntable rotation speed from 985.58 μrad/s to 968.24 μrad/s. The curve is a fit to a damped harmonic oscillator. Such fits determined the angular deflection scale, $\tau_{\rm torsion}$ and $\tau_{\rm decay}$. Since the moment of inertia of the pendulum was known, the fit also determined κ and thus the torque scale as well.

signal, and tiny imperfections in the pendulum led to small 1ω, 2ω, and 3ω gravitational torques as well. We therefore fitted the angular deflection data with a Fourier series (to account for real external torques on the pendulum) plus a power series (to account for slow drifts in the equilibrium angle of the fiber).

$$\bar{\theta} = \sum_{m=0}^{m_{\rm drift}} b_m(\bar{\theta})^m + \sum_{n=1}^{n_{\rm harmonic}} [a_n^{\rm sin}\sin(-n\bar{\theta}) + a_n^{\rm cos}\cos(-n\bar{\theta})] \ . \quad (8)$$

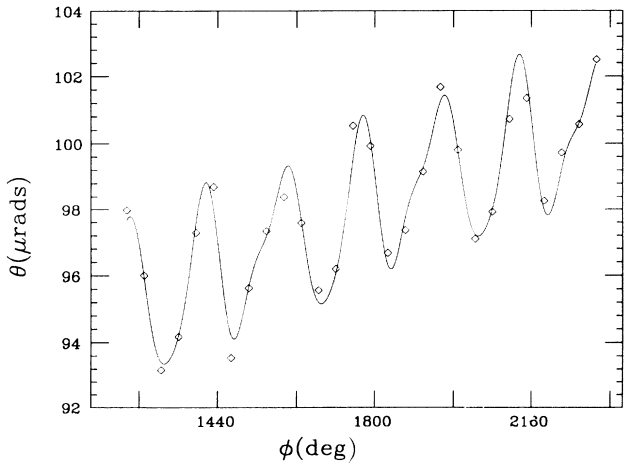

FIG. 9. Typical averaged angular deflection data showing the angular deflection θ as a function of can angle ϕ. These results correspond to the raw data shown in Fig. 7. A 2ω signal from pendulum imperfections is visible. (Note that a positive *difference* coresponds to a negative θ.)

We obtained best results by breaking our data up into runs containing exactly three can periods and fitting the results with $m_{\rm drift}$=3 and $n_{\rm harmonic}$=4. (The results were fairly insensitive to this choice, but it seemed to give the smallest scatter in the extracted $a_1^{\rm sin}$ and $a_1^{\rm cos}$ coefficients.) Small corrections to the a_1 coefficients were applied for the attenuation and phase shift introduced by the lock-in rolloff, the free torsional resonance of the pendulum, and the averaging procedure.

B. Calibrations

The most important calibrations were of the torsional constant κ of our fiber, and of the angular deflection θ. We determined that $\kappa = 30.7 \times 10^{-3}$ ergs/rad from the calculated moment of inertia of the pendulum $\mathcal{J} = 401.2 \pm 0.5$ g cm^2 for Be/Al, and the measured period of free torsional oscillations $\tau_{\rm torsion} = 718 \pm 0.5$ s. The angular deflection was calibrated by four independent means: (1) by rotating the top of the torsion fiber through a known angle using the rotation stage; (2) by translating the position-sensitive photodetector through a known distance using the translation stage (this was particularly well suited for checking the linearity of the detector response); (3) by observing the pendulum angular deflection caused by an abrupt, well-defined change in ω as shown in Fig. 10 (this dynamic calibration was particularly well suited for an absolute calibration of the deflection); and (4) by applying a known gravitational hexadecapole torque to the pendulum as shown in Fig. 11 (this was particularly useful as a check on the entire instrument and on the signal extraction procedure). These four different calibrations gave consistent results. The

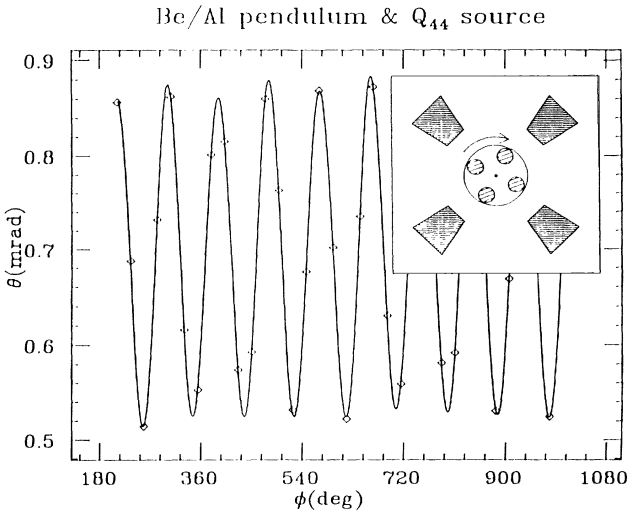

FIG. 11. Test of the torque calibration using the known $\overline{q}_{44}$ moment of the pendulum. A Q_{44} field was generated by four 29-kg Pb blocks configured to maximize the $l = 4, m = 4$ signal. The curve is a Fourier fit to the data. The fitted 4ω amplitude of 176 ± 0.6 μrad agrees with the predicted value of 170 μrad, given our 3% uncertainty in the source strength. Inset: Top view of the detector and source with the detector magnified by a factor of 2.

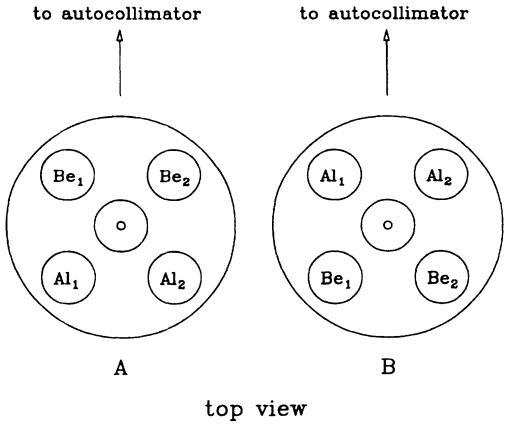

FIG. 12. Mirror image configurations of the test bodies used in the terrestrial source experiments.

accuracy of method 1 was limited to ≈25% because the angle of the top fiber attachment was known to ~0.5 mrad, and the useful span of our photodetector was ≈2 mrad. Methods 2 and 3 were reproducible to ≈1% and agreed with each other at this level. The accuracy of method 4 was limited to ≈3% by uncertainties in the strength of the hexadecapole source resulting from possible errors in the positions and homogeneities of the Pb blocks.

IV. TERRESTRIAL SOURCE EXPERIMENTS

A. Experimental method

We distinguished torques of interest from spurious effects by taking data with the two mirror-image configurations $\mathcal{A}$ and $\mathcal{B}$ of the four test bodies on the pendulum support tray (see Fig. 12). Our signal $\mathbf{S} = [\mathbf{a}_A(1\omega) - \mathbf{a}_B(1\omega)]/2$ was the difference in the 1ω Fourier amplitudes in the $\mathcal{A}$ and $\mathcal{B}$ configurations. This procedure essentially eliminated any spurious signals from gravity gradients or magnetic effects because these tracked the orientation of the pendulum tray rather than the test bodies themselves (see below). In addition, it was effective in eliminating spurious effects from coherent irregularities in the turntable drive because these, too, were independent of the configuration of the masses, as we demonstrate in Fig. 13.

Prior to taking terrestrial source data we adjusted the Helmholtz coils to null the magnetic field at the center of the apparatus. We removed the two inner magnetic shields (leaving the outer shield in place to homogenize the fields from the turntable bearing) and, using a fluxgate magnetometer, reduced the field to 0.2 mG at the location of the middle shield. We then reassembled the apparatus and adjusted the gravity gradient compensator to null the gravity gradient at the pendulum c.m. using the method described in Sec. IV D 5 below.

Before each data run began, we (1) leveled the turntable if the measured tilt exceeded 5 μrad, (2) returned the light spot to the center of the detector (by rotating the top of the fiber) if the *difference* signal was more than ~ 350 μrad away from null, and (3) "pumped down" the torsional amplitude if it exceeded ~ 125 μrad in amplitude. This was done by lowering and raising the

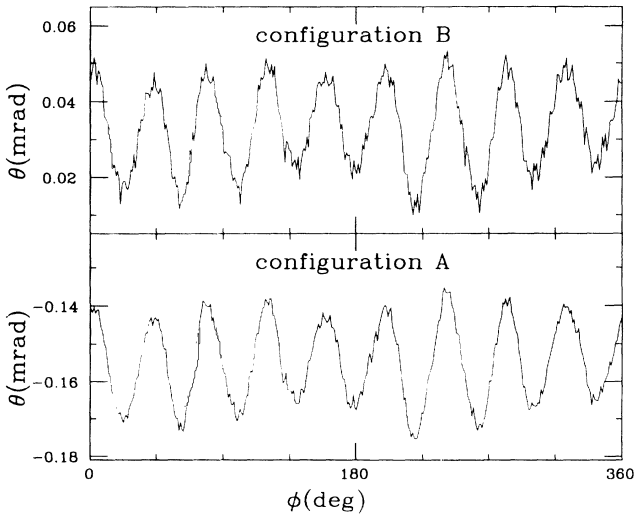

FIG. 13. Demonstration of the reproducibility of turntable irregularities. Our $\tau_{can} = 9\tau_{torsion}$ Be/Cu angular deflection data have been sorted into bins according to the value of ϕ. Coherent angular deflections pumped by turntable irregularities are readily apparent. Lower (upper) panel: data with the pendulum in the $\mathcal{A}$ ($\mathcal{B}$) configuration.

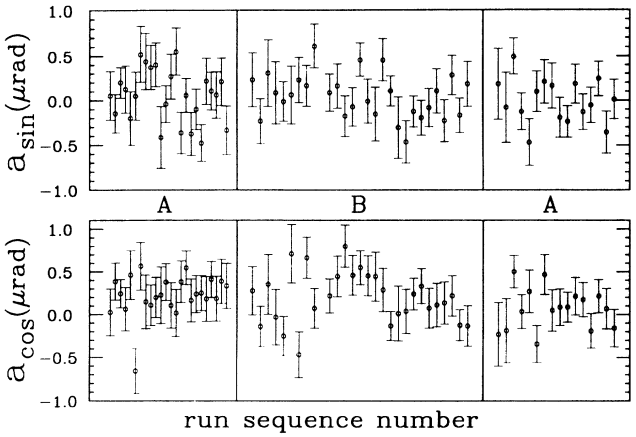

FIG. 14. Be/Al data taken with $\tau_{\text{can}} = 10\tau_{\text{torsion}}$ showing quadrature components of the 1ω angular displacement of the pendulum for test bodies in the $\mathcal{A}$ and $\mathcal{B}$ configurations. The small net vertical offset, independent of configuration, is due to the 1ω component of the coherent turntable drive irregularities. The points have been corrected for tilt.

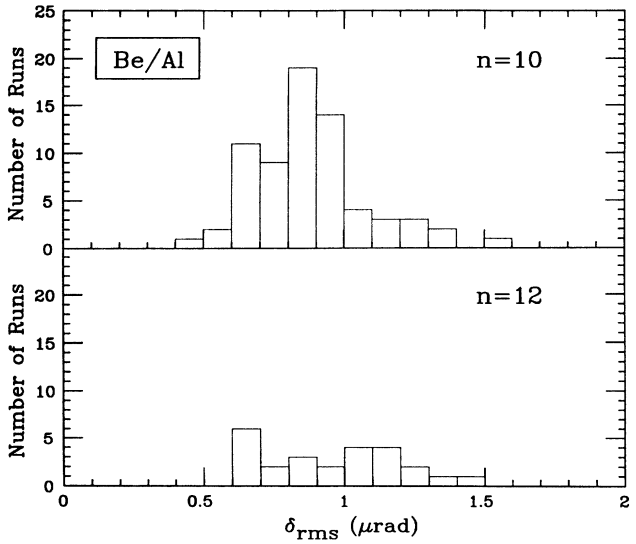

FIG. 15. Histogram of fit residuals for the Be/Al runs. The horizontal axis is the rms residual per degree of freedom.

turntable speed at appropriate points in the torsional cycle.

After each change of the pendulum configuration we checked for magnetic and gravity gradient effects by taking data with the Helmholtz coils off, and then with the gravity gradient compensator reversed to add to the Q_{21} hill gradient.

The terrestrial source data reported here are identical to those presented in Ref. 19. The analysis here, however, uses more refined algorithms and supercedes that of Ref. 19. There is no significant change in the results.

B. The Be/Al comparison

We took Be/Al data at two different turntable speeds corresponding to $\tau_{\text{can}} = n\tau_{\text{torsion}}$ with n=10 and 12, and switched configurations twice in an $\mathcal{AABBBA}$ pattern. The 1ω amplitudes extracted from our angular deflection data are shown in Fig. 14 and summarized in Table I. The data consist of 93 three-cycle runs. A histogram of the rms fit residuals per degree of freedom (DF), δ_{rms}, defined by

$$\delta_{\text{rms}} = \sqrt{\frac{\sum_{i=1}^{N}[\theta_i - \overline{\theta}(\phi_i)]^2}{N-m}}\,, \tag{9}$$

for these runs is shown in Fig. 15. Here N is the number of data points in a three cycle run (typically 30) and m=12 is the number of adjustable parameters in the fitting function. None of the data were discarded on the basis of their rms residuals. However one run was rejected because of a temperature anomaly: the temperature sensor at the autocollimator base showed an exceptionally large 1ω amplitude (3.5 ± 0.5 mK).

TABLE I. Summary of Be/Al data. Deflection amplitudes in nrad. $\mathcal{A}$ and $\mathcal{B}$ refer to the test body configurations. The n=12 data were taken between the $\mathcal{B}1$ and $\mathcal{B}2$ n=10 data.

n	amp	$\mathcal{A}$ 1	$\mathcal{B}$ 1	$\mathcal{B}$ 2	$\mathcal{A}$ 2	O	S
10	$a_1^{\sin}$	62 ± 62	126 ± 57	-35 ± 76	1 ± 62	38 ± 32	-7 ± 32
10	$a_1^{\cos}$	220 ± 50	277 ± 90	130 ± 64	67 ± 61	174 ± 34	-30 ± 34
12	$a_1^{\sin}$	-5 ± 87	346 ± 106			170 ± 69	-176 ± 69
12	$a_1^{\cos}$	-5 ± 89	95 ± 110			45 ± 71	-50 ± 71
x[a]	$a_1^{\sin}$					137 ± 59	44 ± 59
x[a]	$a_1^{\cos}$					118 ± 57	40 ± 57
						$a_1^{\sin}$	-21 ± 26
			Combined result:			$a_1^{\cos}$	-17 ± 27

[a]Earlier data (see Ref. 30) with n not fixed at an integral value.

TABLE II. Summary of Be/Cu data. Deflection amplitudes in nrad. $\mathcal{A}$ and $\mathcal{B}$ refer to the test body configurations. The n=7 data were taken before the n=9 data.

n	amp	$\mathcal{A}$ 1	$\mathcal{B}$ 1	$\mathcal{B}$ 2	$\mathcal{A}$ 2	O	S
9	$a_1^{\sin}$	72 ± 37	111 ± 51	76 ± 45	71 ± 54	82 ± 24	-11 ± 24
9	$a_1^{\cos}$	44 ± 61	54 ± 46	-15 ± 51	73 ± 53	39 ± 27	20 ± 27
7	$a_1^{\sin}$	292 ± 63	214 ± 60			253 ± 44	39 ± 44
7	$a_1^{\cos}$	74 ± 45	88 ± 52			81 ± 34	-7 ± 34
						$a_1^{\sin}$	0 ± 21
				Combined result:		$a_1^{\cos}$	10 ± 21

We derived our cumulative value by taking an unweighted average of the results of the three cycle runs. The error is given by the scatter of the results about the mean (a weighted average of the three-cycle data, using the errors given by the least-squares fit of the three-cycle data, gave essentially the same cumulative result.) We combine this present result with data we reported[30] before the turntable was driven by a crystal oscillator. As shown in Table I, we do not see any significant effect that can be ascribed to an external torque on the composition dipole, obtaining $|\mathbf{S}(\mathrm{Al/Be})| = 27 \pm 26$ nrad where the error is statistical. After adding in quadrature the 8 nrad upper limits on systematic errors described in Sec. IV D below, we find $|\mathbf{S}(\mathrm{Al/Be})| = 27 \pm 27$ nrad. This corresponds to $\Delta a_\perp = (2.1 \pm 2.1) \times 10^{-11}$ cm/s^2 ($\Delta\mathbf{a}_\perp$(Be-Al)$= [(-2.0 \pm 2.2)\hat{\mathbf{x}} + (0.9 \pm 2.1)\hat{\mathbf{y}}] \times 10^{-11}$ cm/s^2 where $\hat{\mathbf{x}}$ and $\hat{\mathbf{y}}$ are unit vectors that point east and north, respectively).

C. The Be/Cu comparison

We took Be/Cu data at two different turntable speeds corresponding to $\tau_{\mathrm{can}} = n\tau_{\mathrm{torsion}}$ with n=7 and 9. The pendulum configuration was switched three times in an $\mathcal{ABBAAB}$ pattern. The 1ω amplitudes extracted from our angular deflection data are shown in Fig. 16 and summarized in Table II. The data consist of 123 three-cycle runs. A histogram of the rms fit residuals for these runs is shown in Fig. 17. Only one of the runs had an rms residual greater than 1.5 μrad/NDF and was discarded. Presumably this run was contaminated by a small "glitch" that was not detected by eye. We do not see any significant effect that can be ascribed to an external torque on the dipole. We obtain $|\mathbf{S}(\mathrm{Cu/Be})| = 10 \pm 21$ nrad (statistical error). After adding in quadrature the 7-nrad upper limit on systematic errors (see Sec. IV D) we find $|\mathbf{S}(\mathrm{Cu/Be})| = 10 \pm 22$ nrad, corresponding to $\Delta a_\perp = (0.8 \pm 1.7) \times 10^{-11}$ cm/s^2 ($\Delta\mathbf{a}_\perp$(Be-Cu)$= [(0.7 \pm 1.7)\hat{\mathbf{x}} + (0.3 \pm 1.7)\hat{\mathbf{y}}] \times 10^{-11}$cm/s^2). This corresponds to a 5-μeV limit on the orientation-dependent kinetic energy, $E = \kappa\theta^2/2$, of a macroscopic object.

D. Systematic errors

The most important issue in experiments of the kind we report here is a detailed understanding and suppres-

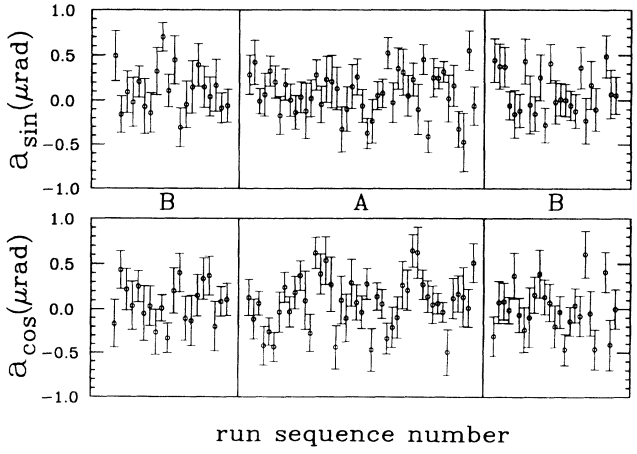

FIG. 16. Be/Cu data taken with $\tau_{\mathrm{can}} = 9\tau_{\mathrm{torsion}}$ showing quadrature components of the 1ω angular displacement of the pendulum for test bodies in the $\mathcal{A}$ and $\mathcal{B}$ configurations. The points have been corrected for tilt.

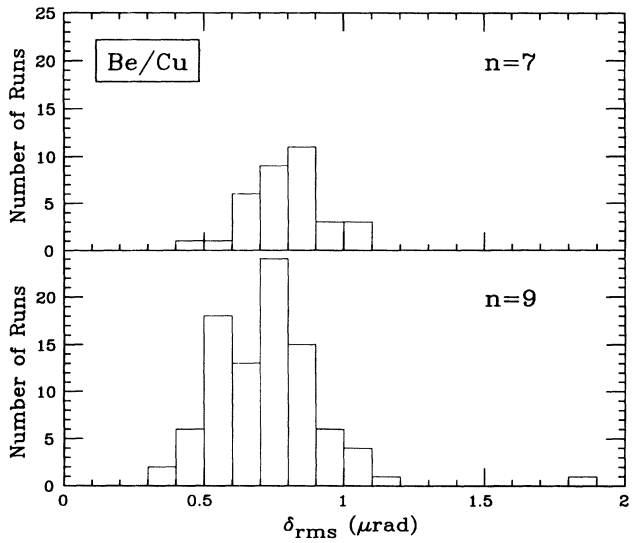

FIG. 17. Histogram of fit residuals for the Be/Cu runs. The horizontal axis is the rms residual per degree of freedom. The single run with a residual of 1.8 μrad was discarded.

TABLE III. Systematic error budget for n=9 Be/Cu data.

Error source[a]	ΔS(nrad)
Turntable (Sec. IV D 1)	≤ 3
Linear tilt correction (Sec. IV D 2)	~ 0.3
Quadratic tilt (Sec. IV D 2)	≤ 0.2
Thermal variations (Sec. IV D 3)	≤ 6
Magnetism (Sec. IV D 4)	≤ 1
Gravity gradients (Sec. IV D 5)	≤ 3
Calibration drifts (Sec. IV D 6)	$\ll 3$
Quadrature sum	≤ 7

[a]Labels in parentheses refer to sections of text where the error is defined.

sion of possible systematic errors. We made careful studies of the most significant effects: coherent turntable irregularities, tilt, thermal variations, magnetic interactions, and gravity gradients. These results are summarized in Table III.

1. Coherent irregularities and noise in the turntable drive

We discovered that coherent irregularities in the turntable drive generated a reproducible pattern of torsional excursions (see Fig. 13). The effect of these irregularities was greatly reduced by setting $\tau_{\rm can}$ to be an integral multiple of $\tau_{\rm torsion}$ (multiples of 7 and 9 gave the best results) and always beginning the averaging process at a definite phase of the torsional cycle. However these driven oscillations were not completely removed by the averaging process and would have led to a spurious 1ω amplitude of up to ≈ 0.5 μrad whose value depended upon ω and on the torsional phase at which the averaging process was begun (see Fig. 18). As long as the turntable irregularities were independent of the orientation of the test bodies on the tray, they would not affect our signal S, but would merely produce an offset, $\mathbf{O} = [\mathbf{a}_A(1\omega) + \mathbf{a}_B(1\omega)]/2$.

In fact, as shown in Table IV, the particular choice of starting phase had no discernable effect on our signal S, although it did affect the offset O. Nonetheless, because the variation of the offset with the starting phase was essentially sinusoidal, this component of the offset could be minimized by extracting the 1ω amplitudes using the

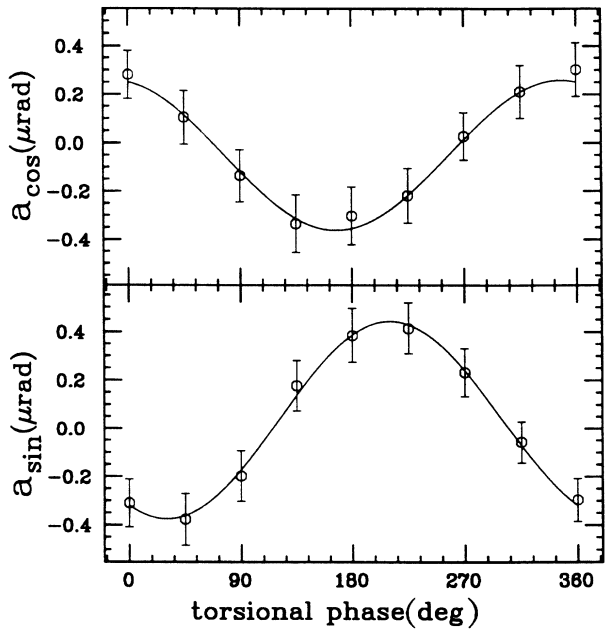

FIG. 18. Extracted 1ω amplitudes as a function of the torsional phase at which the averaging process was begun. The dependences are well described by sinusiods.

following prescription. Each run was averaged twice, at two different starting phases separated by half a torsional period. Each of the two averaged data sets was fitted as described above, and the extracted 1ω amplitudes for a given run were taken to be the averages of the results obtained with the two different starting phases. The results of this analysis were used in the figures and tables above.

As can be seen in Fig. 13, the turntable irregularities were essentially independent of pendulum configuration. Note that the pendulum response is not exactly sinusoidal, but shows evidence for several "kicks" per turntable revolution. Because the dominant pendulum response to impulsive perturbations is at the torsional frequency (i.e., 9ω in the data of Fig. 13), we estimate an upper limit on the systematic error due to long-term *drifts* in turntable irregularities as follows. We determine how much these could have drifted by computing the magnitude and phase of the dominant 9ω component of the $\mathcal{A}$ and $\mathcal{B}$ data shown in Fig. 13. The magnitudes agree to within $(1.8 \pm 1.2)\%$ and the phases to within

TABLE IV. Effect of starting the analysis at differing values of the torsional phase ϕ_t. Be/Cu data with n=9. Deflection amplitudes in nrad. $\mathcal{A}$ and $\mathcal{B}$ refer to test body configurations.

ϕ_t	amp	$\mathcal{A}$ 1	$\mathcal{B}$ 1	$\mathcal{B}$ 2	$\mathcal{A}$ 2	O	S
0°	$a_1^{\sin}$	-118 ± 37	-96 ± 58	-116 ± 49	-124 ± 52	-114 ± 25	-8 ± 25
	$a_1^{\cos}$	-24 ± 61	-30 ± 44	-88 ± 51	-5 ± 54	-37 ± 26	22 ± 26
180°	$a_1^{\sin}$	262 ± 41	317 ± 49	270 ± 43	266 ± 58	279 ± 24	-15 ± 24
	$a_1^{\cos}$	114 ± 63	138 ± 52	59 ± 53	151 ± 56	116 ± 28	17 ± 28

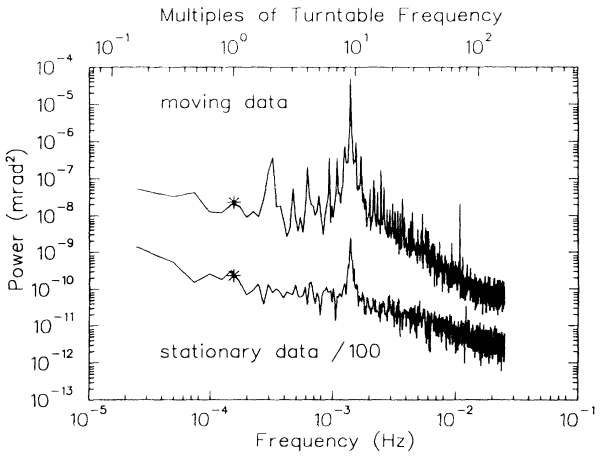

FIG. 19. Power spectrum of the raw *difference* signal with the apparatus stationary and rotating at $n = 9$. Each plot is an average of five equal length ($\approx$ 11 h) 2048 point transforms. The stationary data have been divided by 100 to separate the two curves. A linear background was subtracted from both sets of raw data before generating the Fourier transform. The two "starred" points at 1ω represent the scatter in the $a(1\omega)$ coefficients obtained from our standard analysis.

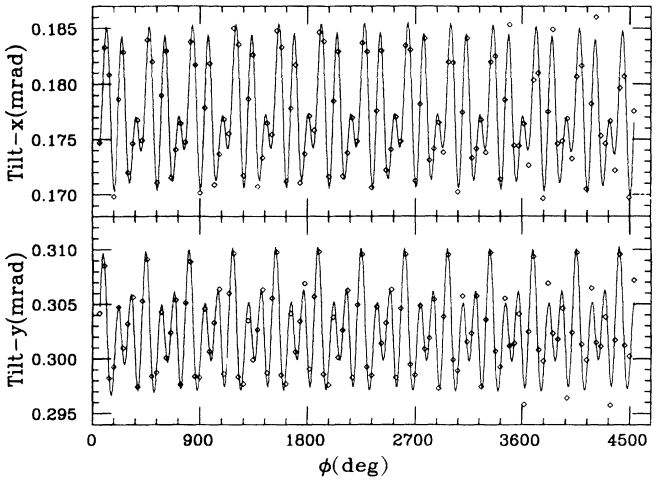

FIG. 20. Tilt signals from two orthogonal sensors mounted on the can lid. Data points are averaged over one torsional period. The curve is a power series plus Fourier series fit to the averaged data. The 1ω tilt for this data is 1.4 ± 0.1 μrad. The signals are dominated by 2ω and 3ω tilts with amplitudes of 3.5 and 5.0 μrad, respectively.

0.11°. We obtain an upper limit $\Delta S \leq 3$ nrad on systematic errors for n=9 Be/Cu data from pumped oscillations by multiplying the observed offset O=91 nrad by 0.03.

The effect of the turntable drive on the pendulum is best seen by a Fourier transform of the raw data. In Fig. 19 we plot the power spectrum of our angular deflection signal obtained with the turntable stationary and rotating at n=9. The stationary data are dominated by $1/\sqrt{f}$ noise plus a peak at $1/\tau_{\text{torsion}}$. Rotating the turntable increases the power at $1/\tau_{\text{torsion}}$ and generates sidebands at other n (typically n=3 to 15). The peak at n=2 is a real torque on the pendulum due to a slight $\overline{q}_{22}$ imperfection in the pendulum. The figure also displays points at 1ω obtained by scaling the uncertainties in the $a(1\omega)$ coefficients from our standard analysis of the n=9 Be/Cu data. These agree well with the Fourier spectra for the can rotating and the can stationary. These results demonstrate that the can rotation has no discernable effect on the noise power at the 1ω signal frequency.

2. Tilt

The turntable was leveled with sufficient accuracy (the rms and mean tilts during data taking were 5.5 and 1.2 μrad, respectively) that spurious signals from tilt were comparable to our "statistical" errors. The tilt signals from a typical run are shown in Fig. 20. The instantaneous rotation axis of the turntable wobbles significantly at 3ω, but the pattern is very stable in time and the 1ω tilt can be adjusted to very small values.

The sensitivity to tilt was found by deliberately tilting the entire apparatus about two orthogonal axes. We found that a tilt of 261 μrad induced a spurious angular deflection of 6.06 ± 0.11 μrad as shown in Fig. 21. We then corrected our three-cycle runs for residual tilt by assuming that the tilt-induced angular deflection was linear in the residual tilt. The uncertainties in the tilt

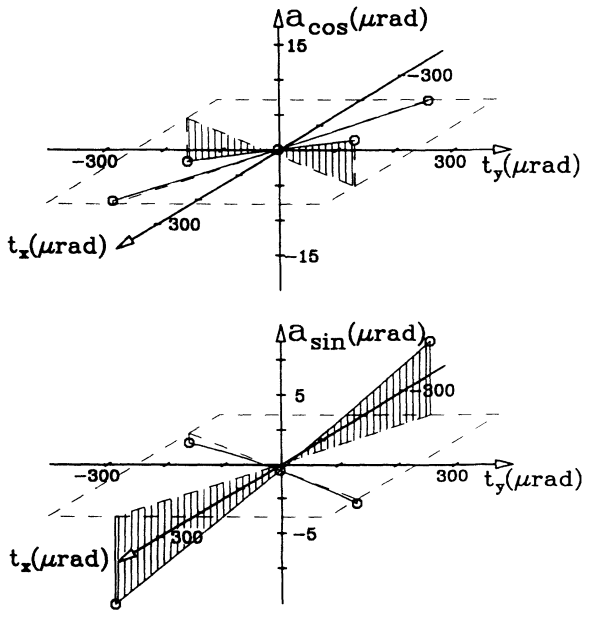

FIG. 21. Tilt sensitivity measurements. The induced 1ω angular deflection is plotted as a function of tilt (t_x, t_y) deliberately introduced along two orthogonal axes.

correction due to uncertainties in the measured residual tilt were added in quadrature to the fluctuating error assigned to each run. We estimate the *systematic* error due to tilt as follows. First, the uncertainty in the *linear* correlation between tilt and deflection was accounted for by multiplying the net tilt correction to an entire data set by the fractional uncertainty in the correlation coefficient. The resulting uncertainty was ≈ 0.5 nrad. An upper limit on errors in the tilt correction procedure itself was estimated using the data of Fig. 21 to find an upper limit on any *quadratic* component of tilt-induced angular deflection and multiplying this coefficient by the square of the rms tilt. The resulting upper limit on this systematic error is negligible (≤ 0.2 nrad).

3. Thermal effects

Thermal data from a typical run are shown in Fig. 22. The dominant variations are slow drifts. To investigate thermal effects we deliberately varied temperatures by amounts much larger than those encountered in normal operation and observed the induced change, δa, in the 1ω amplitude. Thermal systematic errors were derived under the (presumably conservative) assumption that they were linear in the temperature perturbations. Specifically we note the following.

(1) Modulating the room temperature by ± 1.4 K at 1ω (long-term average modulation under normal conditions was 1 mK) gave δa=2.0 μrad. This corresponds to a systematic error under normal conditions of $|\Delta S| \approx 1.4$ nrad.

(2) Modulating the shield temperature by ± 0.6 K at 1ω (long-term average under normal conditions was 0.2 mK) gave δa=9.6 μrad. This corresponds to a systematic error under normal conditions of $|\Delta S| \approx 4$ nrad.

(3) Taking isothermal data with the shields 0.5 K above and below the normal operating temperature of 296.5 K (long-term stability was 10 mK) gave $\delta a \leq 0.25$ μrad. This corresponds to a systematic error under normal conditions of $|\Delta S| \leq 2.5$ nrad.

(4) Isolating one upper quadrant of the thermal shield and raising its temperature by $\approx$ 10°C with a 20-W heater gave $\delta a \leq 0.5$ μrad. We estimated that the maximum correlated temperature difference of one quadrant under normal conditions was $\approx$ 0.03°C by determining the temperature change induced in a thermal shield panel when one of six mounting screws was removed (all screws were in place under normal conditions). The corresponding systematic error under normal operating conditions is $|\Delta S| \leq 3$ nrad.

(5) Attaching the 20-W heater to the rotating apparatus gave $\delta a \leq 0.5$ μrad (actual power dissipated by rotating electronic components was $\approx$0.5 W). This corresponds to $|\Delta S| \leq 1$ nrad under the conservative assumption that the power dissipation did not vary by more than 10% during normal data taking.

We checked our assumption that thermal effects were linear in the perturbation by reducing the shield modulation by a factor of 2.9 and observing that the induced 1ω signal dropped by a factor of 3.3 ± 1.1.

Our thermal tests were conducted at residual gas pressures of $\approx$1 Torr, where the viscosity was essentially independent of pressure (see Fig. 5). Because the thermal conductivity of a rarified gas is proportional to its viscosity, which was shown to be essentially constant for the pressures of interest, we judged it sufficient to perform these tests at a typical residual gas pressure. Note that the operating pressures were nearly identical for the $\mathcal{A}$ and $\mathcal{B}$ configuration data. After each configuration change $\approx$4 days elapsed before equivalence principle data taking began, during which the pressure would rise to $\approx$0.2 Torr. When vacuum was broken for the next configuration change the pressure was between $\approx$1 and $\approx$1.5 Torr.

The tests discussed above established that systematic errors from thermal effects were less than 6 nrad. We also searched for correlations in the normal data between the 1ω autocollimator signal and the average value or the 1ω amplitude (< 1 mK for sensors on the apparatus) of any of the seven temperature sensors. No significant correlations were observed.

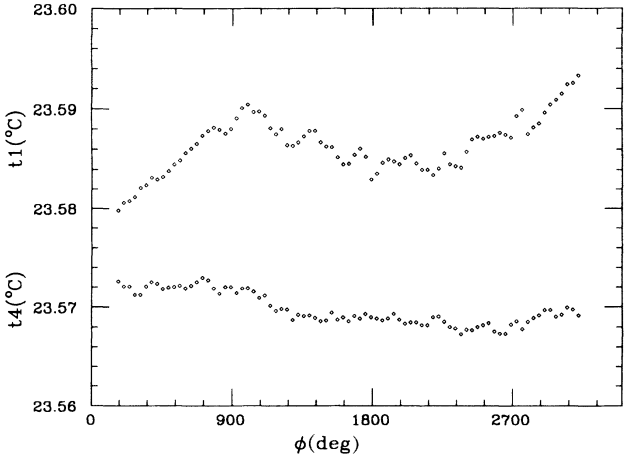

FIG. 22. Temperature signals for a typical run. Points contain data averaged over τ_{torsion}. The $t1$ sensor was at the base of the autocollimator, $t4$ was a stationary sensor mounted on the turntable.

4. Magnetic interactions

Magnetic effects were studied by measuring the induced 1ω amplitudes when the instrument was operated under the following conditions: (1) normal pendulum, magnetic shields in place, Helmholtz coils off ($|\delta \mathbf{a}| \leq 0.2$ μrad); (2) normal pendulum, magnetic shields removed, Helmholtz coils off [$\delta \mathbf{a} = (-154\hat{i} - 287\hat{j})$ μrad for Be/Cu masses]; (3) pendulum with test bodies removed, magnetic shields removed, Helmholtz coils off [$\delta \mathbf{a} = (-149\hat{i} - 286\hat{j})$ μrad]. These tests determined the attenuation factors of our shields and revealed that the

pendulum had a small (48×10^{-6} erg/G) magnetic moment which was unaffected, to within $(3.0 \pm 0.6)\%$ for Be/Al and $(1.6 \pm 0.5)\%$ for Be/Cu, by removing the test bodies. The magnetism was therefore located in the pendulum tray. Although this moment generated a 1ω amplitude of ≤ 20 nrad when the Helmholtz coils were on, it did not produce a spurious result because the magnetic moment was virtually unaffected by switching between the $\mathcal{A}$ and $\mathcal{B}$ configurations. This was confirmed by taking data with the Helmholtz coils off, after each test body interchange. Magnetic effects, therefore, gave an insignificant contribution (< 1 nrad) to our error budget.

5. Gravity gradient couplings

Gravity gradient effects were studied by replacing the normal test bodies with special gradiometer bodies. These gradiometer bodies had the same outside dimensions, masses and Au surfaces as the normal test bodies, but their c.m.'s were displaced ± 4.0 mm from their geometrical centers by making one end cap of Al and the other of Cu. These gradiometer bodies gave the pendulum a calculable $\overline{q}_{21}$ of 24.15 g cm^2 (and a small $\overline{q}_{41}$), and allowed us to measure precisely the dominant Q_{21} gradient of the hill (see Fig. 23). This gradient was then reduced from its ambient value by a factor of 145 with the compensating Q_{21} mass distribution discussed in Sec. II C 4. After each change of the pendulum configuration, the residual $\overline{q}_{21}$ moment of the normal pendulum was measured by rotating the Q_{21} compensator by 180° about the vertical axis so that it doubled rather than cancelled the ambient gradient, producing a Q_{21} gradient ≈ 290 times greater than that encountered in ordinary operation. From the observed $|\delta a| \approx 1.4$ μrad, we inferred a residual $\overline{q}_{21} = (0.057 \pm 0.005)$ g cm^2. This corresponded to one of the test bodies being vertically displaced by 27 μm, and produced a 1ω amplitude under normal operating conditions of < 10 nrad. However, the gravity gradient effect was found to be independent of the configuration of the test bodies on the tray, and to correlate with a small warp in the tray. The gravity gradient contribution to our signal S essentially canceled when subtracting data from the $\mathcal{A}$ and $\mathcal{B}$ configurations, and generated an insignificant contribution (< 3 nrad) to our error budget.

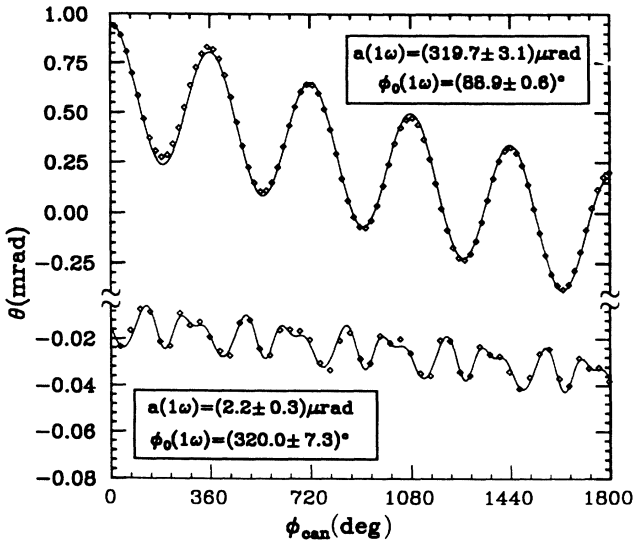

FIG. 23. Gravity gradient compensation. The upper curve shows the gradiometer signal from the ambient gravity gradient in the laboratory. The lower curve shows the gradiometer signal after the gradient compensator was installed. The compensator reduced the 1ω signal by a factor of 145. A small 2ω amplitude from pendulum imperfections is now apparent.

6. Calibration drifts

Because our analysis procedure involves subtracting 1ω amplitudes for $\mathcal{A}$ and $\mathcal{B}$ configurations, each of which has an "offset," we could infer a spurious signal if the angular displacement scale varied between the two configurations. We took data (for example, in the sequence $\mathcal{BAAB}$) in such a fashion that any *linear* drifts in the calibrations would cancel. Furthermore, repeated calibration checks showed no evidence for any significant calibration drifts. For example, a dynamic calibration of the angular deflection scale taken just before beginning the data shown in Fig. 16 agreed to 3% with one taken just after the end of this data. Because configuration changes did not affect the optics in any way, we assert that the mean calibration for the $\mathcal{A}$ data agreed with that for the $\mathcal{B}$ data to $\ll 3\%$. [Indirect evidence for the calibration stability comes from the $(1.8 \pm 1.2)\%$ agreement of the 9ω amplitudes in the $\mathcal{A}$ and $\mathcal{B}$ configuration data shown in Fig. 13.] Since the offsets in this data were less than 100 nrad, any systematic errors due to calibration fluctuations are $\ll 3$ nrad.

E. Fundamental limit from thermal fluctuations

Fluctuations in the thermal energy of the pendulum set a fundamental limit on the accuracy attainable from any torsion balance. Boynton[31] has shown that thermal fluctuations produce an uncertainty in the angular displacement

$$\delta\theta_{\rm rms}^{\rm thermal} = \sqrt{\frac{6kT}{\mathcal{J}\tau_{\rm decay}\Delta t}}\left(\frac{\tau_{\rm torsion}}{2\pi}\right)^2 , \qquad (10)$$

where k is Boltzmann's constant, T the temperature, and Δt is the duration of the experiment. Using $\tau_{\rm decay}$=3800 s (corresponding to $Q \approx 17$), and values for $\tau_{\rm torsion}$ and $\mathcal{J}$ given above, we find that for our Be/Cu measurement ($\Delta t \approx 2 \times 10^6$ s) $\delta\theta_{\rm rms}^{\rm thermal} \approx 3$ nrad, which is ≈ 7 times smaller than our observed fluctuating error of 22 nrad. The excess "random" scatter of our data points is presumably dominated by seismic noise and residual temperature fluctuations.

F. Constraints on new interactions

An interaction mediated by scalar bosons differs significantly from one due to vector exchange. The spin of the exchanged boson affects both the sign of α_5 and the form of q_5. The α_5 coefficient is negative for a scalar interaction and positive for a vector force. The fundamental distinction between scalar and vector charges is illustrated by their differing types of behavior under charge conjugation. The scalar charge of a particle is identical to that of its antiparticle, while the vector charge of particle and antiparticle have opposite signs. These symmetries naturally affect the dependence of the scalar and vector charges upon the binding energy of ordinary matter as well. Therefore, in presenting implications of our upper limits on the differential acceleration of Be and Al, and of Be and Cu in the field of the Earth, we consider separately the cases of vector and scalar interactions.

1. Vector Yukawa interactions

The most general form of the vector charge of stable, electrically neutral matter[32] is

$$q_5 = B\cos(\theta_5) + L\sin(\theta_5)\ . \tag{11}$$

where B and L are the two apparently conserved, but "unused," baryon and lepton quantum numbers, and θ_5 is a mixing angle that specifies the vector charge. In this parameterization, charges proportional to B, L, $B-L$, or $3B+L$ correspond to θ_5=0, 90, −45, or 18.4 degrees, respectively.

The differential acceleration of a test body pair due to this potential is

$$\begin{aligned}\Delta\mathbf{a} = {} & \alpha_5 G[\Delta(B/\mu)\cos(\theta_5) + \Delta(L/\mu)\sin(\theta_5)] \\ & \times[\mathbf{I}_B(\lambda)\cos(\theta_5) + \mathbf{I}_L(\lambda)\sin(\theta_5)]\ ,\end{aligned} \tag{12}$$

where $\Delta(B/\mu)$ and $\Delta(L/\mu)$ are the differences in baryon and lepton densities of the "detector" test bodies, and $\mathbf{I}_B$ and $\mathbf{I}_L$ are gradients of integrals of the baryon and lepton densities over the "source" (the Earth); for example

$$\mathbf{I}_B(\lambda) = -\nabla_{r_1}\int \rho(\mathbf{r}_2)\frac{B}{\mu}(\mathbf{r}_2)\frac{e^{-|\mathbf{r}_1-\mathbf{r}_2|/\lambda}}{|\mathbf{r}_1-\mathbf{r}_2|}d^3r_2\ . \tag{13}$$

The differential charges of our two detectors can be obtained from the values $\Delta(B/\mu)_{\text{Cu-Be}} = 2.468\times10^{-3}$, $\Delta(L/\mu)_{\text{Cu-Be}} = 1.262\times10^{-2}$, $\Delta(B/\mu)_{\text{Al-Be}} = 2.036\times10^{-3}$, and $\Delta(L/\mu)_{\text{Al-Be}} = 3.797\times10^{-2}$.

We evaluated $\mathbf{I}_B(\lambda)$ and $\mathbf{I}_L(\lambda)$ in two regimes. For 1 m$\leq\lambda\leq$20 km the integrals were evaluated in terms of a multipole expansion of the Yukawa potential

$$\begin{aligned}T_5(\phi) &= \kappa\bar{\theta}(\phi) \\ &= 4\pi i\alpha_5 G\sum_{l=0}^{\infty}\frac{1}{2l+1}\sum_{m=-l}^{+l} m\,\bar{q}^5_{lm}Q^5_{lm}e^{-im\phi}\ ,\end{aligned} \tag{14}$$

where

$$\bar{q}^5_{lm} = \int\frac{q_5}{\mu}(\mathbf{r})_{\text{det}}\rho_{\text{det}}(\mathbf{r})\,\lambda^l(2l+1)!!i_l\left(\frac{r}{\lambda}\right)Y^*_{lm}(\hat{\mathbf{r}})\,d^3r \tag{15}$$

is evaluated in the body-fixed frame centered on the pendulum c.m., and

$$\begin{aligned}Q^5_{lm} = \int\frac{q_5}{\mu}(\mathbf{r})_{\text{source}}\rho_{\text{source}}(\mathbf{r})\frac{1}{\lambda^{l+1}(2l-1)!!}k_l\left(\frac{r}{\lambda}\right) \\ \times Y_{lm}(\hat{\mathbf{r}})\,d^3r\end{aligned} \tag{16}$$

is evaluated in the laboratory frame. Here i_l and k_l denote modified spherical Bessel functions.[33] (With these definitions $\bar{q}^5$ and Q^5 approach the gravitational $\bar{q}$ and Q in the limit where $\lambda\to\infty$.)

The Q^5 integrals were computed using measurements of the laboratory building and detailed topographic maps of the surrounding territory out to a radius of 40 km. Conventional topographic maps gave the elevation of the soil (assumed to have a density of 2.2 g/cm^2) and the depth of the surrounding bodies of water. The depth of the soil-rock interface was obtained from U.S. Geological Survey (USGS) data;[34] the rocks were assumed to have a density of 2.7 g/cm^2. Possible deeper lying density contrasts were ignored. The relative contribution to $\mathbf{I}_B$ and $\mathbf{I}_L$ from the relatively poorly known soil-rock interface is greatest at large values of λ. At λ = 20 km the *magnitude* of this contribution equals that of the air-soil interface. However the *directions* of the two contributions differ by $\approx 60°$, so that subsurface topography gives a negligible contribution to the magnitudes of the source integrals, which are the quantities of most importance in interpreting our null results. The $\mathbf{I}_B(\lambda)$ source integral for $\lambda\leq 20$ km is shown in Fig. 24.

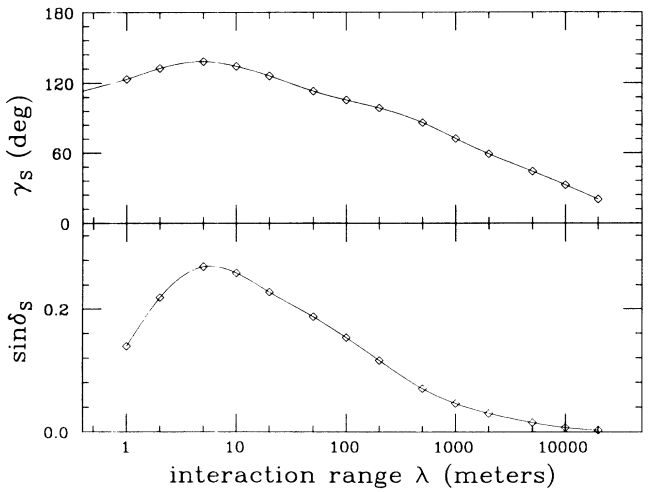

FIG. 24. Source integrals for the Eöt-Wash site. We assume $q_5 = B$ and display the λ dependence of $\sin\delta_s \equiv |\mathbf{I}_B|/(2\pi\rho_0\lambda)$ and $\gamma_s \equiv \arctan(I_E/I_N)$ where ρ_0=2.2 g/cm^2 and E and N refer to the easterly and northerly components of $\mathbf{I}_B$. The angle δ_s is the inclination of an "infinite" plane of density ρ_0 that produces the same $\mathbf{I}_B$ as the actual source; γ_s is the azimuthal angle of the Yukawa force vector.

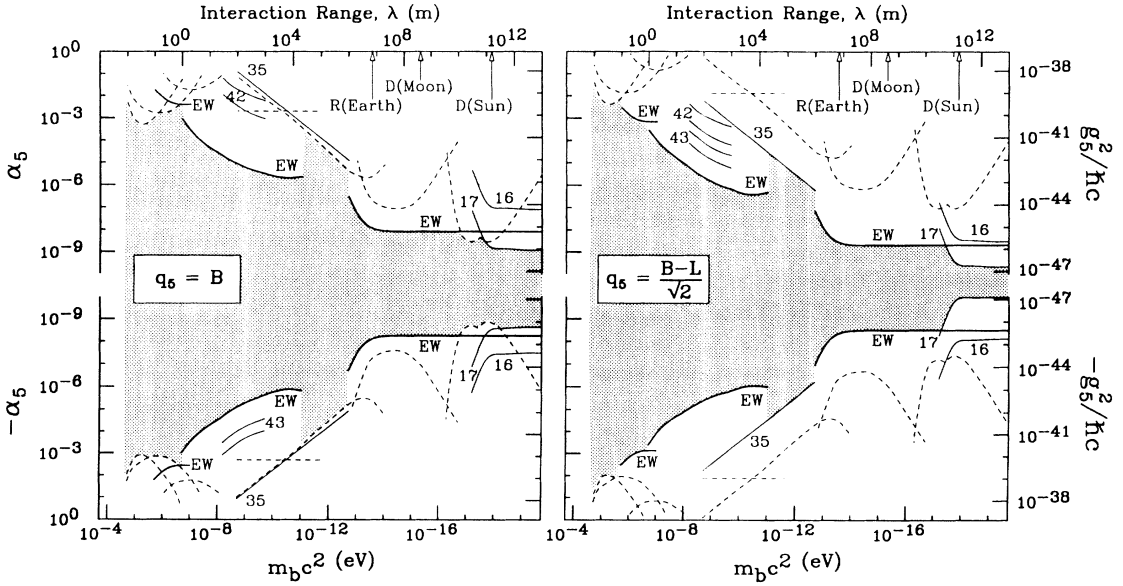

FIG. 25. 2σ constraints on interactions of ultra-low-mass vector bosons from this and previous experiments. Upper limits on α_5, or g_5^2, as a function of boson mass $m_b c^2$, or range λ. Although one expects α_5 to have a positive sign corresponding to the repulsive vector interaction between like charges, for simplicity in interpreting experimental results which can have either sign we consider the possibility of negative α_5 as well. Dashed curves are from tests of the $1/r^2$ law. The horizontal dashed constraints are from Ref. 40; the remaining dashed curves from work summarized in Ref. 39. Solid curves are from composition dependence experiments; numbers on the curves correspond to references in the text. Left panel: $q_5 = B$; right panel: $q_5 \propto B - L$. The curves labeled EW are from this work.

We do not quote the source integrals for 20 km $< \lambda <$1000 km because at this length scale uncertainties from possible deeper lying density contrasts have a relatively large effect on the horizontal components of **I** to which our device is sensitive. Therefore, in this regime the most sensitive constraints come from Galileo-type experiments.[35,36]

For $\lambda \geq$1000 km we computed the integrals using a layered, ellipsoidal model of the Earth which assumes that the Earth is in isostatic equilibrium under gravitational and centrifugal forces. The density profile and chemical composition of the Earth were taken from Refs. 37 and 38, respectively.

Our constraints on interactions of ultra-low mass bosons are shown in Figs. 25 and 26, along with those deduced from previous inverse square law[39,40] and composition-dependence studies. Figure 25 shows constraints on interactions coupled to B and to $(B-L)/\sqrt{2}$ (corresponding to $\theta_5 = 0°$ and $\theta_5 = -45°$) as a function of λ. The constraints on $q_5 = (B-L)/\sqrt{2}$ interactions from the solar Eötvös and $1/r^2$ experiments assume[41] that 73% of the Sun's mass is hydrogen and the remainder is $N = Z$ material. Figure 26 shows constraints on α_5 as functions of θ_5 for λ fixed at 100 m. Note that the constraint on α_5 from each differential acceleration result has two poles[42]—one at the value of θ_5 where Δq_5 of the detector vanishes and another where q_5 of the source vanishes. We used two different dipoles (Be/Cu and Be/Al) to eliminate the detector pole. A laboratory source experiment that removes the source pole will be discussed below.

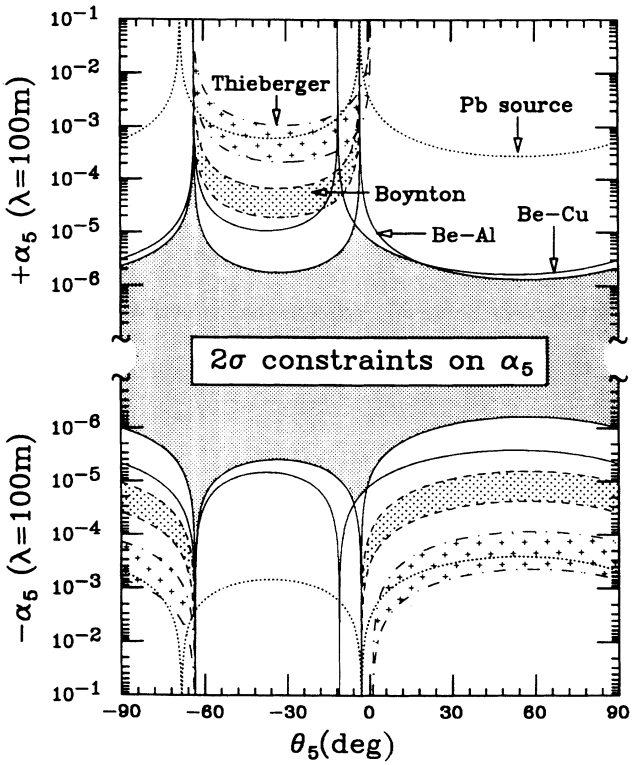

FIG. 26. Constraints on α_5 as a function of mixing angle θ_5 for a vector interaction with an assumed range λ=100 m. The dotted curve labeled *Pb source* is from our laboratory source experiment described below. The heavily shaded region is allowed by our results. For comparison, we show constraints corresponding to the positive results reported by Thieberger (Ref. 43) and Boynton *et al.* (Ref. 44).

Our results are more sensitive than previous data for most of the region from $\lambda \geq 1$ m to $\lambda \leq 1$ AU, and represent improvements by up to a factor of 300 over previous limits. As can be seen in Figs. 25 and 26 we are in strong disagreement with the positive effects observed by Thieberger[43] and Boynton *et al.*,[44] if these are interpreted as arising from a single Yukawa interaction[45] coupled to any linear combination of B and L, except for a very restricted region around $\theta_5 \approx -63°$. This region will be discussed in Sec. V below. We are, of course, consistent with the less stringent null results reported by Roll *et al.*,[16] Niebauer *et al.*,[35] Fitch *et al.*,[46] Speake and Quinn,[47] Cowsik *et al.*,[48] Bennett,[49] Kuroda, and Mio,[36] and Bizzeti *et al.*[50]

Searches for vector bosons that couple to B or L are of continuing interest in particle physics. Hawkins and Perl[51] discuss constraints from $g_e - 2$, $e^+e^- \rightarrow e^+e^-$ and beam dump experiments on a particle L that couples only to leptons, and consider future experiments to extend the results to higher masses. We show their constraints along with those from our data in Fig. 27. Nelson and Tetradis[52] discuss constraints on a boson, B, that couples to quark ($= B/3$) number. If the B couples only to baryon number, then it will be stable for masses $m_B \leq m_\pi$. We show their most sensitive constraints (from $\pi^0 \rightarrow B\gamma$ and $\eta \rightarrow B\gamma$ and n-Pb scattering) in Fig. 27 along with those from our work.

Much of the recent interest in searching for finite-range violations of the equivalence principle was stimulated by the reanalysis[6] by Fischbach *et al.* of the von Eötvös data. In Fig. 28 we add our points to the plot presented in that paper.

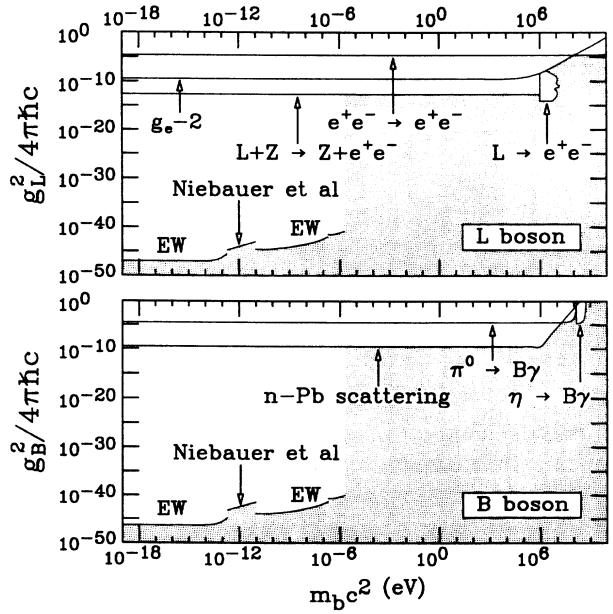

FIG. 27. 2σ constraints on the couplings of proposed L and B bosons coupled to L and B, respectively. The vertical axes display coupling strengths defined in Eq. (1). The curves labeled EW are from this work.

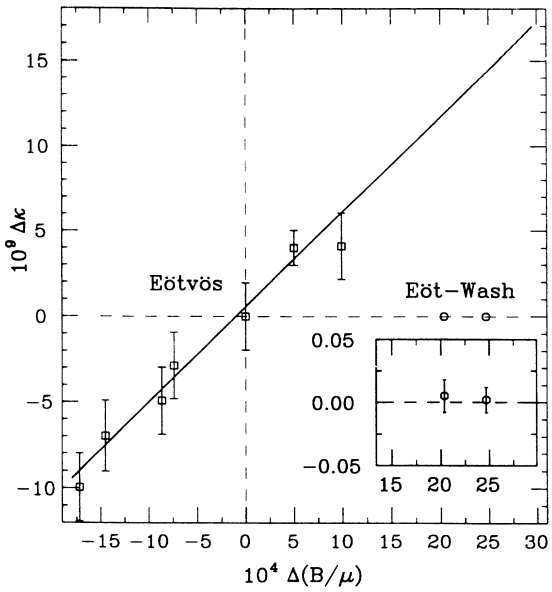

FIG. 28. Updated version of the plot presented in Ref. 6. Our points are added to the reanalyzed von Eötvös data. The inset has the vertical scale magnified by a factor of 100 in order to show the error bars of our data.

2. *Scalar Yukawa interactions*

It is difficult to specify the scalar charges of various materials as these depend on results of detailed calculations using specific models. For example, one possible charge would be the expectation value $m_q\bar{q}q$ which reflects the number of quarks plus antiquarks in the nucleus. Although the scalar couplings may be simple in terms of the fundamental fields, the total scalar charge of a neutral atom will reflect the structure of atoms and nuclei and will, in general, depend on the atomic and nuclear quantum numbers in a complicated way. We therefore follow the ideas of Peccei, Sola, and Wetterich[9] and characterize the scalar charge phenomenologically as

$$q_5 \approx (\mu + \epsilon_B|B| + \epsilon_L|L|) \tag{17}$$

and expect that $|\epsilon_B|$ and $|\epsilon_L|$ are both $\ll 1$. In effect, Peccei *et al.* argue that the primary coupling of a scalar is to mass, with small substance-dependent corrections that can be approximated by terms linear in $|B|$ and $|L|$. In this case all sources are expected to have $q_5 \approx \mu$, so that the differential acceleration toward an external source will be

$$\Delta\mathbf{a} \approx \alpha_5 G[\epsilon_B \Delta(B/\mu) + \epsilon_L \Delta(L/\mu)]\mathbf{I}_B(\lambda) \; . \tag{18}$$

In Fig. 29 we plot constraints on $\alpha_5\epsilon_B$ and $\alpha_5\epsilon_L$ for an interaction with λ=100 m. By comparing Figs. 26 and 29 one can see that the main qualitative difference between the scalar and vector constraints is that the source pole is absent in the former because (assuming $|\epsilon_B| \ll 1$ and $|\epsilon_L| \ll 1$) the scalar charge of the source cannot vanish.

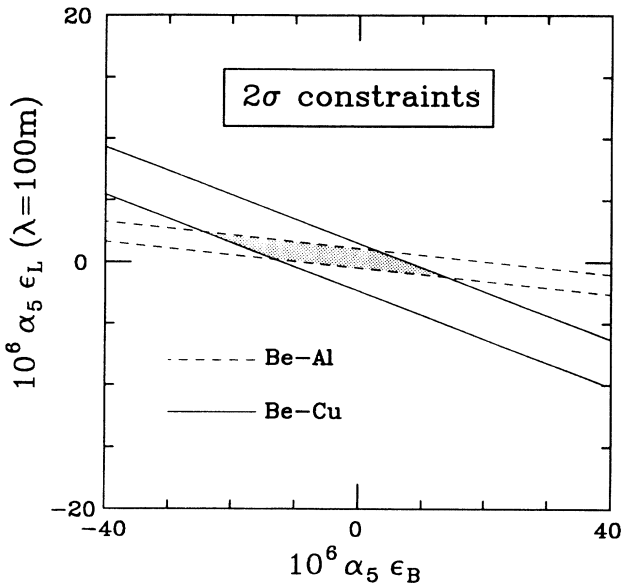

FIG. 29. Constraints on interactions of ultra-low-mass scalar bosons from this experiment.

3. Quantum-gravity inspired scalar-vector interactions

Goldman, Hughes, and Nieto[8] (GHN) have extensively discussed the possibility that there exist scalar and vector partners of the conventional tensor graviton, and that these could lead to attractive and repulsive Yukawa interactions of roughly gravitational strength between test bodies consisting of ordinary matter:

$$V_{12}(r) = \left[-\alpha_S \left(\frac{q_S}{\mu}\right)_1 \left(\frac{q_S}{\mu}\right)_2 e^{-r/\lambda_S} + \alpha_V \left(\frac{q_V}{\mu}\right)_1 \left(\frac{q_V}{\mu}\right)_2 e^{-r/\lambda_V} \right] G\frac{m_1 m_2}{r} . \tag{19}$$

GHN conjectured that the gravi-scalar and gravi-vector potentials essentially cancel in experiments with ordinary matter, and recommend testing this idea by studying the gravitational properties of anti-matter, in particular by comparing the gravitational acceleration of protons and antiprotons. The antiproton-Earth vector interaction has the opposite sign of the proton-Earth vector interaction, while the scalar interactions would be the same. Because the scalar and vector forces on the antiproton add, GHN argue that an antiproton experiment at the 1% level would provide a useful result. In this subsection we discuss constraints that can already be placed on this difference from our own data, from recent interferometric Galileo-type experiments,[35,36] and from tests of the $1/r^2$ law summarized in Ref. 39 plus the recent work of Ref. 40. Our constraints are obtained under the assumption (implicit in the work of GHN) that the gravi-vector interaction does not couple to electric charge.

Our reasoning, in a nutshell, is this. If antiprotons and protons fall with different accelerations in the Earth's field, it must be due to a vector interaction whose charge can be taken to be B. The p-$\bar{p}$ acceleration difference, from such a gravi-vector is expected to be proportional to $\Delta(B/\mu, p/\bar{p}) \approx 2$. This same vector interaction leads to a Cu-Be acceleration difference approximately 1000 times smaller, $\propto \Delta(B/\mu, \text{Be/Cu}) \approx 2.5 \times 10^{-3}$. However we determine the Be/Cu "gravitational" acceleration difference to a precision of ≈ 1.0 part in 10^{11}, which more than makes up for our weaker effect. The only subtle issue concerns possible cancellation of the gravivector interaction by the gravi-scalar interaction in the Eöt-Wash results. It is important to note that such cancellation *cannot* be exact. Because of the inherently different properties of scalar and vector charges under the charge-conjugation operator, binding energy must give different contributions to the gravivector and graviscalar charges.

Let us consider the various possibilities. First suppose that, contrary to expectation, the graviscalar interaction coupled exactly to mass ($\epsilon_B = \epsilon_L = 0$). Then differential acceleration experiments would see only the gravivector interaction and the constraints on α_V from our work and the Galileo experiments[35,36] (see Figs. 25 and 26) are better than those one could obtain from a 1% measurement of $g_{\bar{p}}$ by a factor which ranges from 1×10^3 to 5×10^8, depending on the value of λ_V.

Next suppose that $|\epsilon_B|$ and $|\epsilon_L|$ are $\ll 1$ as expected. Then to have a graviscalar interaction whose composition dependence essentially cancels a gravivector force large enough to be detected in an 1% antiproton experiment, α_S must be so large that it would easily have been detected in tests of the $1/r^2$ law. Recall that for the graviscalar interaction, $1/r^2$ tests probe α_S while differential acceleration experiments probe $\alpha_S[\epsilon_B \Delta(|B|/\mu) + \epsilon_L \Delta(|L|/\mu)]$. Thus the graviscalar and gravivector forces cannot cancel in *both* differential acceleration and $1/r^2$ experiments. For example, a 1% difference in g between protons and antiprotons [$\Delta(B/\mu) = 2$] implies a gravivector differential acceleration of the Cu and U test bodies [$\Delta(B/\mu) = 7.1 \times 10^{-4}$] in the Colorado Galileo experiment[35] of $\Delta a = 3.6 \times 10^{-6} g$. The Colorado null result, $\Delta a \leq 5 \times 10^{-10} g$, requires the graviscalar differential acceleration to be $-3.6 \times 10^{-6} g$. Let us assume that $|\epsilon_B| \approx 0.01$. This requires an α_S about 10^6 times larger than the limit set by the Earth–Moon–Laser Geodynamics Satellite (-LAGEOS) $1/r^2$ test summarized in Fig. 25.

Finally, suppose that $|\epsilon_B|$ and $|\epsilon_L|$ are ≥ 1. At this point our approximate expression for the scalar charge (linear in $|B|$ and $|L|$), is no longer valid. Even if, by some remarkable chance, the graviscalar and gravivector interactions canceled, say, in a differential acceleration experiment with Be/Al, they would not cancel in a Be/Cu measurement. If, for example, the scalar and vector charge differences of test body pairs with mass number ratios varying over a factor of ≈ 3 failed to "track" each other by only 1%, then one of our measurements, ei-

ther Be/Al or Be/Cu, would have shown an effect $\approx 10^4$ times larger than our quoted upper limit.

Furthermore, our results by themselves place very tight restrictions on the parameters of *any* two-Yukawa model. We have recently shown[53] that the complicated topography of our site produces a Yukawa force whose direction is a strong function of λ (see Fig. 24). This leads to strong constraints on two-Yukawa models simply because two forces of different range, and correspondingly different directions, cannot cancel. If the two Yukawa interactions had ranges ≤ 20 km and roughly gravitational strength, our null results require these ranges to be identical to a high degree of accuracy, as we show in Fig. 30.

We therefore conclude that the quantum-gravity-inspired model of GHN cannot accommodate an antiproton gravitational acceleration that differs from g by more than 1 part in 10^5. A more detailed account of the arguments summarized in this subsection has been submitted for publication elsewhere.[54]

4. Test of the equivalence principle

When interpreted as a test of the equivalence principle in the field of the Earth, our 1σ results correspond to

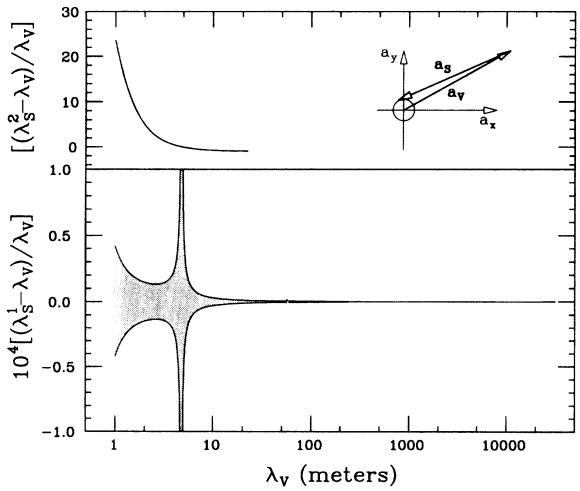

FIG. 30. Constraints from our Be/Cu data on parameters of a proposed "quantum gravity" model in which the gravivector interaction couples to B with $\alpha_V=1$. The allowed difference $\Delta\lambda = \lambda_S - \lambda_V$ is shown as a function of λ_V. Because our source integrals (see Fig. 24) have a maximum at $\lambda \approx 5$ m, there are two solutions denoted by λ_S^1 and λ_S^2. The 1σ regions consistent with our data are shaded. Top panel: solution 1; the allowed region is much smaller than the width of the line. The inset shows how the gravivector and graviscalar accelerations must lie within our error circle. Bottom panel: solution 2. Within either allowed region the constraints are satisfied only for a very narrow range of α_S/α_V. For example, at $\lambda_V = 10$ km, the product $\alpha_S\Delta(q_S/\mu)_{\rm det}\,(q_S/\mu)_{\rm source} I_S$ must lie within ≈ 1 part in 10^6 of the corresponding vector quantity.

$$m_i/m_g(\mathrm{Cu}) - m_i/m_g(\mathrm{Be}) = \frac{\Delta a_{\rm south}}{g\sin\delta} = (0.2 \pm 1.0) \times 10^{-11} \quad (20)$$

and

$$m_i/m_g(\mathrm{Al}) - m_i/m_g(\mathrm{Be}) = \frac{\Delta a_{\rm south}}{g\sin\delta} = (0.5 \pm 1.3) \times 10^{-11} \,. \quad (21)$$

This improves on previous tests in the field of the Earth (see discussion in Ref. 16) by about a factor of 400. Compared to limits on $\delta m/m$ in the field of the Sun, our Be/Cu result is a little more precise than that obtained by Roll *et al.*[16] (1σ error in $\delta m/m = 1.5 \times 10^{-11}$), but significantly poorer than that claimed by Braginsky and Panov[17] (1σ error $= 0.45 \times 10^{-12}$). It may be worth noting that the ratio of atomic masses used in our work (Cu:Be) is quite similar to those of the solar experiments (Au:Al or Pt:Al).

5. Implications for testing the strong equivalence principle

Laboratory experiments test only the "weak" form of the equivalence principle; they cannot determine if gravitational binding energy itself falls with acceleration g because gravitational binding energy makes a negligible contribution to the mass of laboratory-sized objects. The "strong" principle can be tested by comparing the acceleration of the Earth and Moon in the field of the Sun because the masses of these bodies are large enough to have a significant contribution from gravitational binding (gravitational binding energy reduces the mass of the Earth by ≈ 5.1 parts in 10^{10}). Analyses[55,56] of lunar laser ranging data through 1976 have established that the Earth and Moon fell toward the Sun with accelerations that were identical to 14 parts in 10^{12} (95% confidence). More refined analyses including subsequent data are expected to lower this limit to ≈ 1 part in 10^{12}.

Nordtvedt[57] has pointed out that to take full advantage of this precision it is necessary to rule out the unlikely possibility that a composition-dependent interaction approximately cancels a gravitational binding energy anomaly. Because, in general, any given pair of test bodies may accidentally have a vanishing "charge" difference, at least two laboratory equivalence principle experiments with quite different test bodies are required to rule out the possibility of a composition-dependent interaction effect on the Earth-Moon differential acceleration toward the Sun. The Princeton and Moscow solar equivalence principle experiments have very similar test bodies and, in this respect, are not really independent. However by combining the Al/Au and Al/Pt solar results with our Be/Cu and Be/Al data, we can place rigorous upper limits on the possible contribution of composition-dependent interactions to the Earth-Moon differential acceleration. We discuss the case of a vector interaction (which must couple to a linear combination of B and L) in detail. Using accepted values for the elemental compositions of the Sun,[41] Earth,[37,38] and Moon,[58] we deduce

$$(B/\mu)_{\rm Earth} = 1.000759\ , \quad (L/\mu)_{\rm Earth} = 0.4869\ , \qquad (22)$$

$$(B/\mu)_{\rm Moon} = 1.000603\ , \quad (L/\mu)_{\rm Moon} = 0.4942\ , \qquad (23)$$

$$(B/\mu)_{\rm Sun} = 0.9942\ , \quad (L/\mu)_{\rm Sun} = 0.8592\ , \qquad (24)$$

and compute, as a function of the mixing angle θ_5, the maximum differential acceleration of the Earth and Moon allowed by the Princeton, Moscow, and Eöt-Wash results (see Fig. 31). At 2 σ, the largest $\Delta a/a = \Delta m/m$ consistent with our results and those of RKD and Braginsky and Panov is $\approx 5 \times 10^{-12}$ and $\approx 1.5 \times 10^{-12}$, respectively. Thus the solar and terrestrial Eötvös experiments combined with the 1976 lunar ranging results rigorously verify that gravitational binding energy accelerates in a gravitational field at the same rate as other forms of mass-energy to a precision of better than 3% (95% confidence level). Our limit on nongravitational Earth-Moon acceleration differences is sufficiently good that one can take full advantage of the expected results of new analyses of the lunar-ranging data.

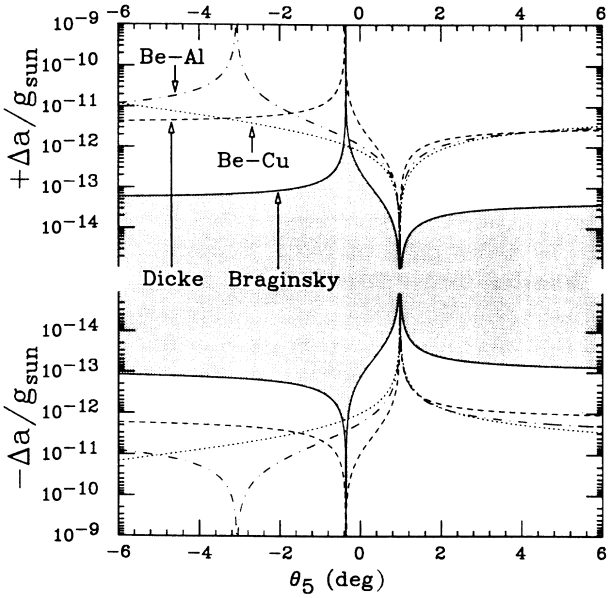

FIG. 31. Maximum contribution of a $\lambda = \infty$ vector interaction to the Earth-Moon differential acceleration toward the Sun, showing 2σ constraints from our Be/Cu and Be/Al data, and the RKD and Braginsky-Panov solar Eötvös experiments. The zero occurs because the earth-moon charge difference vanishes at $\theta_5 \approx 1°$. The poles occur at values of θ_5 where the charge difference vanishes for the Al/Au and Al/Pt test body pairs used in the RKD and Braginsky-Panov experiments. Outside the range of this plot, the upper limits on $\Delta a/a$ from the solar experiments are essentially independent of θ_5; the Eöt-Wash constraint has a zero at $\theta_5 \approx -49°$ where the charge of the Sun vanishes. The joint constraints for any value of θ_5 are thus at least as stringent as those shown on this plot. Note that the gravitational binding energy of the Earth is 5.1×10^{-10} of its mass.

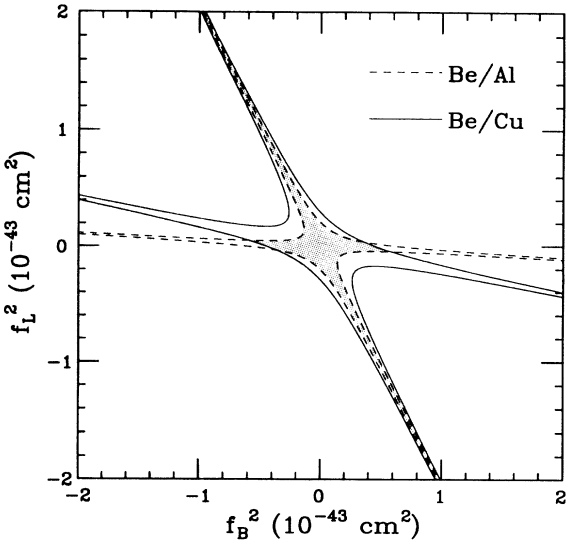

FIG. 32. 1 σ constraints on the parameters f_B^2 and f_L^2 of Moffat's nonsymmetric theory of gravity as analyzed by Will.

A more detailed presentation of the material in this section will appear elsewhere.[59]

6. *Moffat's nonsymmetric theory of gravity*

Moffat[60] has developed a non-symmetrical gravity theory that predicts composition dependent interactions which do not have a Yukawa form. We follow Will's[61] recent analysis of this theory[62] to obtain constraints on its parameters from our data. The constraints on the parameters f_B^2 and f_L^2 obtained from our Be/Al and Be/Cu data are shown in Fig. 32. These constraints are roughly an order of magnitude tighter than those from Will's analysis of the Colorado Galileo experiment.

V. A LABORATORY SOURCE EXPERIMENT

A. Motivation

As can be seen in Fig. 26, all results obtained with terrestrial sources are fairly insensitive to an interaction whose charge is proportional to $B - 2L = N - Z$, simply because such sources contain essentially equal numbers of neutrons and protons and are effectively neutral.[52] To remove this "blind spot," and to check on evidence for an interaction coupled to $N - Z$ presented by Boynton *et al.*,[43] we conducted an experiment using a laboratory source having a substantial neutron excess.

B. Experimental method

These data were taken before the terrestrial source data discussed above and some refinements to the ap-

paratus, particularly to the turntable and to the magnetic and thermal shielding, had not yet been implemented. The outermost layer of the magnetic shield had not been installed and a Au-plated Cu electrostatic shield was used instead of the innermost mu-metal shield. The hermetic thermal shielding was in place but its temperature was not actively controlled. The turntable was "homemade." The main bearing consisted of a ground brass plate that slid on a lubricated, ground stainless steel surface. The turntable was driven through 50 000:1 reduction gearing by a stepper motor with a resolution of 200 steps/revolution. Except for the worm gear itself, the turntable was constructed entirely from nonferromagnetic materials. The stepper motor was driven by a voltage-controlled oscillator instead of by the oven-stabilized crystal used in the terrestrial source experiments.

The key to this measurement was a moveable source that had appreciable strength for Yukawa interactions with $q_5 \propto B - 2L$, and yet produced very small gravitational torques on the pendulum (see Fig. 33). The source was made of Pb which has $(N - Z)/(\text{volume}) \approx 120$ times that of the rock source used by Boynton *et al.* The source had two sections. The inner section, consisting of 215 kg of machined blocks positioned on 19.4-cm-radius tracks, was located within the thermal shield. This section spanned 180° of azimuth and was centered vertically on the pendulum c.m. By symmetry all Q_{lm} with even m vanish and only those Q_{l1}'s with odd l are nonzero. The lowest moment that could cause trouble, Q_{31}, was reduced by tailoring the Pb distribution as a function of polar angle. The outer section of the source, consisting of 1080 kg of bricks positioned with an accuracy of ±2 mm, was located outside the thermal shielding. This section, which had reflection symmetry about a horizontal plane through the pendulum c.m., roughly doubled the strength of the source for interactions with $\lambda \geq 1$ m. Symmetry considerations guaranteed that the Q_{lm} moments of the outer source vanished if $l - m$ was odd. The Q_{11} moment of the entire source was 1802 kg m^{-2}.

The source could be moved between two positions denoted by $\mathcal{A}$ and $\mathcal{B}$. The source in position $\mathcal{A}$ was the mirror image (reflected about a vertical plane passing through the detector c.m.) of the source in position $\mathcal{B}$. The $\mathcal{A}$ and $\mathcal{B}$ sources established a Q_{11}^5 moment that pointed alternately $\approx 45°$ or $\approx 225°$ away from the dominant Q_{21} gravity gradient from the hillside. Because we were able to modulate the source we did not need to be concerned with torques that were fixed in the laboratory. Hence it was not necessary to cancel the Q_{21} gradient as was done in our terrestrial source work. Instead we eliminated its effect by subtracting results taken in the $\mathcal{A}$ and $\mathcal{B}$ configurations. This also eliminated any problems from coherent drive irregularities, etc., so we did not need to reconfigure the test bodies on the tray.

We switched the source between $\mathcal{A}$ and $\mathcal{B}$ three times. After each source change we releveled the turntable, and did not resume taking data until sufficient time had elapsed to equilibrate the internal temperatures. We also took data with the source absent to check that the average of the $\mathcal{A}$ and $\mathcal{B}$ data was consistent with the data taken when the source was removed.

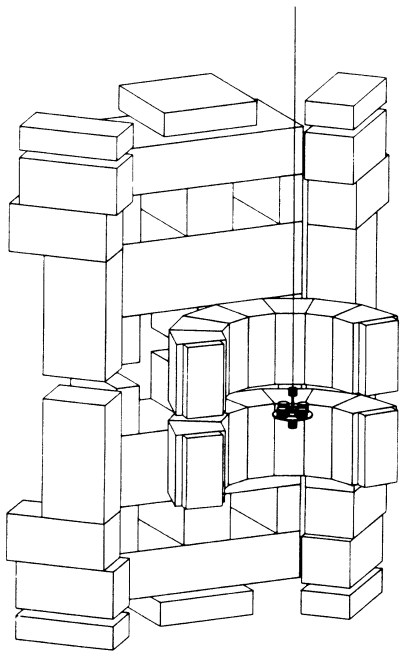

FIG. 33. The Pb source experiment. The inner and outer elements of the Pb source are shown to scale, along with the torsion pendulum.

C. Results

The $a_1^{\sin}$ and $a_1^{\cos}$ coefficients from 25 individual measurements (see Fig. 34) were fitted in terms of

$$a_1^{\sin} = A_{\text{Pb}} \cos(\Phi_{\text{Pb}}) + A_{\text{lab}} \cos(\Phi_{\text{lab}}) \ , \tag{25}$$

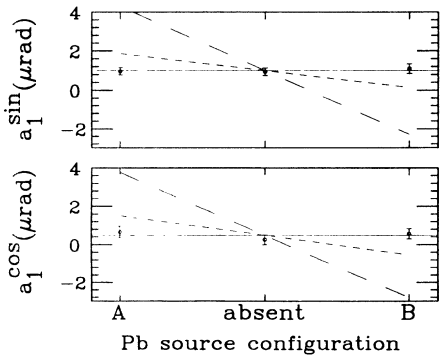

FIG. 34. Quadrature components of the 1ω angular deflection with the Pb source absent, and in the A and B configurations. Each point is based on at least 31 complete rotations of the apparatus. The short-dashed and long-dashed lines show the expected signal of the proposed interaction of Boynton *et al.* for ranges of 100 and 1000 m, respectively.

$$a_1^{\cos} = A_{\rm Pb}\sin(\Phi_{\rm Pb}) + A_{\rm lab}\sin(\Phi_{\rm lab})\ , \qquad (26)$$

where $A_{\rm Pb}$ is an arbitrary amplitude whose phase $\Phi_{\rm Pb}$ tracked the Pb source, and $A_{\rm lab}$ and $\Phi_{\rm lab}$ account for any effects that are independent of the source configuration (for example gravity gradient effects, coherent turntable irregularities, etc.). The phase $\Phi_{\rm Pb}$ is known. The other three parameters are varied to minimize χ^2. We did not observe a significant signal from the source ($A_{\rm Pb} = -0.02 \pm 0.17$ μrad). The laboratory signal ($A_{\rm lab} = 1.10 \pm 0.14$ μrad, $\Phi_{\rm lab} = 26°$) is consistent with the expected gravity gradient and turntable drive effects. The uncertainties are determined by the scatter in the 25 individual measurements.

Expressed as a difference in acceleration of Be and Al toward the Pb source, our results are $a(\mathrm{Be}) - a(\mathrm{Al}) = (-0.15 \pm 1.31) \times 10^{-10}$ cm s^{-2}.

D. Systematic errors

Small tilt corrections were applied as discussed in Sec. IV D 2 above. The largest correction to any of the points in Fig. 34 was only 0.03 μrad. Because the source position was modulated in this measurement, the only important errors were those which tracked the signal and also reversed when the source was moved from $\mathcal{A}$ to $\mathcal{B}$. Two mechanisms were of particular concern: Q_{l1} gradients from the source, and magnetic fields generated by the source.

Although the symmetry of the source and detector nominally ensure that $m = 1$ torques enter only in $l \geq 5$ order, a combination of small imperfections in both the source and the detector could produce a $\overline{q}_{21}Q_{21}$ torque that could mimic a new interaction. The residual $\overline{q}_{21}$ moment of the pendulum was measured by configuring the inner source to produce a known Q_{21} field as discussed in Sec. IV D 5 above. We found that $|\overline{q}_{21}| = (0.067 \pm 0.007)$ g cm^2. This value agreed with that obtained in the terrestrial source experiments, providing additional evidence for our assertion that the stray $\overline{q}_{21}$ moment was a property of the pendulum tray and was unaffected by moving the test bodies. The stray Q_{21} moment of the source was measured using the gradiometer test bodies as discussed above; we found that $Q_{21} = (9.5 \pm 0.9) \times 10^{-3}$ g cm^{-3}. From these two measurements we infer that $A_{\rm Pb}^{\rm grav} = 0.007$ μrad, which is a negligible correction to our results.

We discovered that in the first part of our data, a small (≈ 0.4 mG) change in the ambient magnetic field was correlated with the source reversal. This was traced to three steel screws in the outer source platform. The effect of these screws on our results was assessed by successively replacing the screws with permanent magnets having ≈ 120 or ≈ 38 times greater magnet moments. The magnets were alternately placed at positions corresponding to the $\mathcal{A}$ and $\mathcal{B}$ source positions. These tests showed that the induced 1ω signal was linear in the perturbing field. By scaling the results to the observed $\Delta B = 0.4$ mG, we determined that the spurious effect was negligible ($A_{\rm Pb}^{\rm mag} = 0.02$ μrad).

We tested for thermal influences on our results by searching for any correlation of the $a_1^{\sin}$ and $a_1^{\cos}$ coefficients with the 1ω amplitude from any of the three rotating temperature sensors (typical value ≈ 2 mK), or with the average temperature during a run. No significant correlations were observed.

E. Constraints on Yukawa interactions

Our limits on the differential acceleration of Be and Al towards Pb correspond to

$$\alpha_5(\theta_5 = -63°) = (-0.14 \pm 1.24) \times 10^{-3} \qquad (27)$$

and

$$\alpha_5(\theta_5 = 0°) = (0.21 \pm 1.90) \times 10^{-3}\ , \qquad (28)$$

for $\lambda \gg 1.0$ m. The sensitivity falls for interactions with shorter ranges: for λ=1.0 m, λ=0.3 m, and λ=0.1 m, our limits on α_5 increase by factors of 1.07, 1.56, and 5.04, respectively.

Our 2σ constraints on interactions with $\theta_5 \approx -63°$ are shown in Fig. 35 along with those from other exper-

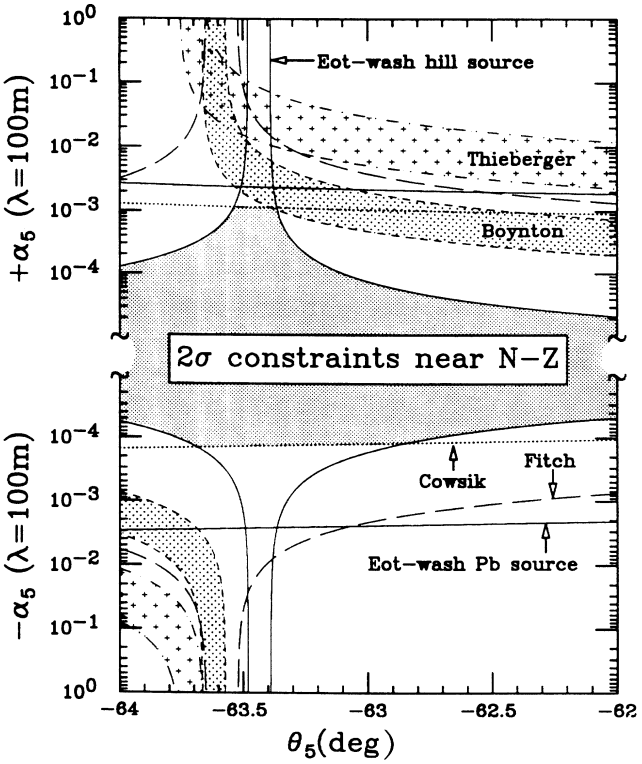

FIG. 35. Constraints on vector interactions coupled predominantly to $B - 2L$ from this and other work. This plot enlarges the region around $\theta_5 = -63°$ shown in Fig. 26. The heavily shaded region is allowed by our work and that of Ref. 63. Uncertainties in the chemical compositions of the different sources were taken from Refs. 44 and 46. This analysis supersedes that in Ref. 18.

iments, including results from the Irvine[63] and Bombay groups[64] published after our results were reported. It is clear that proposed interaction of Boynton *et al.*, which was consistent with all results prior to ours,[18] is ruled out with a very high degree of confidence by a combination of our results with those of Ref. 63.

VI. CONCLUSIONS

We have made a sensitive, systematic search for interactions mediated by ultra-low-mass scalar or vector bosons using two different detector dipoles and two different sources. We find absolutely no evidence for any new interactions ascribable to such particles. Our results break new ground over ranges from roughly 1 AU down to roughly 30 cm, and are considerably more precise than any of those which claim evidence for "new physics."[43,44] Furthermore, none of the experiments that report positive effects have been reproduced, even by the experimenters themselves. Hence we suspect that these positive results are unidentified, subtle experimental artifacts; and that attempts to construct models that can reconcile all the different experiments are not justified.

Finally, it is interesting that our present results, which correspond to a 10^{-29} eV/atom limit on the orientation-dependent energy of our pendulum (10^{-29} eV is less than the electrostatic energy of two electrons 10 000 light years apart) are still well above the ultimate limits (determined by fluctuations in the thermal energy of the pendulum, etc.) of the torsion balance.

ACKNOWLEDGMENTS

Our work profited from the help of many people. Professor E. Fischbach kindled our interest in searching for composition-dependent interactions. Professor F.J. Raab made incisive contributions to early versions of this experiment, particularly to the optics and the data analysis. Professor Y. Fujii and Professor P.G. Bizzeti made valuable suggestions on torsion pendulum design. R. Watanabe wrote the powerful and flexible data acquisition program. P. Williams produced the computer-controlled crystal oscillator for the turntable drive. The skilled and prompt assistance of the Physics Department and Nuclear Physics Laboratory Instrument Shops helped us to make rapid progress. Finally this work was possible only because of support from the National Science Foundation (Grants Nos. PHY-871939 and PHY-8451277), the Department of Energy, and by the University of Washington Physics Department.

---

*Present address: Center for Particle Astrophysics, University of California, Berkeley, CA 94720.

[1] T.D. Lee and C.N. Yang, Phys. Rev. **98**, 1501 (1955).
[2] J. Scherk, in *Unification of Fundamental Particle Interactions*, edited by S. Ferrara, S. Ellis, and P. van Nieuwenhuizen (Ettore Majorana International Science Series Vol. 7) (Plenum, New York, 1980); Phys. Lett. **88B**, 265 (1979).
[3] P. Fayet, Nucl. Phys. **B187**, 184 (1981); Phys. Lett. B **171**, 261 (1986); **172**, 363 (1986).
[4] J.E. Moody and F. Wilczek, Phys. Rev. D **30**, 130 (1984).
[5] D. Chang, R.N. Mohapatra, and S. Nussinov, Phys. Rev. Lett. **55**, 2835 (1985).
[6] E. Fischbach, D. Sudarsky, A. Szafer, C. Talmadge, and S.H. Aronson, Phys. Rev. Lett. **56**, 3 (1986).
[7] A. De Rújula, Phys. Lett. B **180**, 213 (1986).
[8] T. Goldman, R.J. Hughes, and M.M. Nieto, Phys. Lett. B **171**, 217 (1986).
[9] R.D. Peccei, J. Sola, and C. Wetterich, Phys. Lett. B **195**, 183 (1987).
[10] I. Bars and M. Visser, Gen. Relativ. Gravit. **19**, 219 (1987).
[11] J.S. Bell, in *Fundamental Symmetries*, edited by P.B. Bloch, P. Pavlopoulos, and R. Klapisch (Plenum, New York, 1987), p. 1.
[12] C.T. Hill and G.G. Ross, Phys. Lett. B **205**, 125 (1988).
[13] M. Visser, Gen. Relativ. Gravit. **20**, 77 (1988).
[14] S. Nussinov, Phys. Rev. D **38**, 1606 (1988).
[15] C.T. Hill, D.N. Schramm, and J.N. Fry, Comments Nucl. Part. Phys. **19**, 25 (1989).
[16] P.G. Roll, R. Krotkov, and R.H. Dicke, Ann. Phys. (N.Y.) **26**, 442 (1964).
[17] V.B. Braginsky and V.I. Panov, Zh. Eksp. Teor. Fiz. **61**, 873 (1971) [Sov. Phys. JETP **34**, 463 (1972)].
[18] C.W. Stubbs, E.G. Adelberger, B.R. Heckel, W.F. Rogers, H.E. Swanson, R. Watanabe, J.H. Gundlach, and F.J. Raab, Phys. Rev. Lett. **62**, 609 (1989).
[19] B.R. Heckel, E.G. Adelberger, C.W. Stubbs, Y. Su, H.E. Swanson, G. Smith, and W.F. Rogers, Phys. Rev. Lett. **63**, 2705 (1989).
[20] NSG Precision Cells, Inc., Farmingdale, New York.
[21] California Fine Wire Co., Grover City, California.
[22] Model 13031, Oriel Corp., Stratford, Connecticut.
[23] Conetic AA, Perfection Mica Co., Bensonville, Illinois.
[24] Model RTE-210, Neslab Instruments Inc., Portsmouth, New Hampshire.
[25] Model 430, Huber Diffraktionstechnik GMBH, Rimsting, West Germany.
[26] Model HFBR-1522, Hewlett-Packard Corp., Palo Alto, California.
[27] Model LSC-5D, United Detector Technology Inc., Hawthorne, California.
[28] Model 781, Applied Geomechanics Inc., Santa Cruz, California.
[29] Model AD590, Analog Devices Inc., Norwood, Massachussetts.
[30] E.G. Adelberger, in *Tests of Fundamental Laws in Physics*, proceedings of XXIVth Rencontre de Moriond (the IXth Moriond Workshop), Les Arcs, France, 1989, edited by O. Fackler and J. Tran Thanh Van (Editions Frontiéres, Gif-sur-Yvette, 1989), p. 485.
[31] P. Boynton, in *5th Force and Neutrino Physics*, proceedings of the XXIIIrd Rencontre de Moriond (VIIIth Moriond Workshop), Les Arcs, France, 1988, edited by O. Fack-

ler and J. Tran Thanh Van (Editions Frontières, Gif-sur-Yvette, 1988), p. 431.
[32]P. Fayet, Phys. Lett. B **227**, 127 (1989).
[33]G. Arfken, *Mathematical Methods for Physicists*, 3rd ed. (Academic, Orlando, FL, 1985), p. 633.
[34]J. Yount, G. Dembroff, and G. Barats, *Map Showing Depth to Bedrock in the Seattle* 30′ *by* 60′ *Quadrangle* (U.S. Geological Survey No. MS1692, Menlo Park, CA, 1985); J.M. Buchanan-Banks, *Depth to Bedrock in the Tacoma and part of the Centralia* 30′ *by* 60′ *Quadrangles* (U.S. Geological Survey, Menlo Park, CA, preliminary draft).
[35]T.M. Niebauer, M.P. McHugh, and J.R. Faller, Phys. Rev. Lett. **59**, 609 (1987).
[36]K. Kuroda and N. Mio, Phys. Rev. Lett. **62**, 1941 (1989).
[37]A.M. Dziewonsky and D.C. Anderson, Phys. Earth Planet. Inter. **25**, 297 (1981).
[38]J.W. Morgan and E. Anders, Proc. Natl. Acad. Sci. USA **77**, 6973 (1980).
[39]C. Talmadge, J.-P. Berthias, R.W. Hellings, and E.M. Standish, Phys. Rev. Lett. **61**, 1159 (1988).
[40]C. Jekeli, D.H. Eckhardt, and A.J. Romaides, Phys. Rev. Lett. **64**, 1204 (1990).
[41]C.W. Allen, *Astrophysical Quantities* (Athlone, London, 1976), p. 30.
[42]E.G. Adelberger, C.W. Stubbs, W.F. Rogers, F.J. Raab, B.R. Heckel, J.H. Gundlach, H.E. Swanson, and R. Watanabe, Phys. Rev. Lett. **59**, 849 (1987); **59**, 1790(E) (1987).
[43]P. Thieberger, Phys. Rev. Lett. **58**, 1066 (1987).
[44]P.E. Boynton, D. Crosby, P. Ekstrom, and A. Szumilo, Phys. Rev. Lett. **59**, 1385 (1987).
[45]Strictly speaking, this statement applies only to ranges for which Refs. 43 and 44 quote constraints.
[46]V.L. Fitch, M.V. Isaila, and M.A. Palmer, Phys. Rev. Lett. **60**, 1801 (1988).
[47]C.C. Speake and T.J. Quinn, Phys. Rev. Lett. **61**, 1340 (1988).
[48]R. Cowsik, N. Krishnan, S.N. Tandon, and C.S. Unnikrishnan, Phys. Rev. Lett. **61**, 2179 (1988).
[49]W.R. Bennett, Jr., Phys. Rev. Lett. **62**, 365 (1989).
[50]P.G. Bizzeti, A.M. Bizzeti-Sona, T. Fazzini, A. Perego, and N. Taccetti, Phys. Rev. Lett. **62**, 2901 (1989).
[51]C.A. Hawkins and M.L. Perl, Phys. Rev. D **40**, 823 (1989).
[52]A.E. Nelson and N. Tetradis, Phys. Lett. B **221**, 80 (1989).
[53]C.W. Stubbs, E.G. Adelberger, and E.C. Gregory, Phys. Rev. Lett. **61**, 2409 (1988).
[54]E.G. Adelberger, B.R. Heckel, C.W. Stubbs, and Y. Su (unpublished).
[55]J.G. Williams, R.H. Dicke, P.L. Bender, C.O. Alley, W.E. Carter, D.G. Currie, D.H. Eckhardt, J.E. Faller, W.M. Kaula, J.D. Mulholland, H.H. Plotkin, S.K. Poultney, P.J. Shelus, E.C. Silverberg, W.S. Sinclair, M.A. Slade, and D.T. Wilkinson, Phys. Rev. Lett. **36**, 551 (1976).
[56]I.I. Shapiro, C.C. Counselman III, and R.W. King, Phys. Rev. Lett. **36**, 555 (1976).
[57]K. Nordtvedt, Phys. Rev. D **37**, 1070 (1988).
[58]A.E. Ringwood, *Origin of the Earth and Moon* (Springer, New York, 1979), p. 187.
[59]E.G. Adelberger, B.R. Heckel, G. Smith, Y. Su, and H.E. Swanson, Nature **347**, 261 (1990).
[60]J.W. Moffat, Phys. Rev. D **19**, 3554 (1979); **35**,. 3733 (1987).
[61]C.M. Will, Phys. Rev. Lett. **62**, 369 (1989).
[62]R.B. Mann, J.H. Palmer, and J.W. Moffat, Phys. Rev. Lett. **62**, 2765 (1989), have proposed an unorthodox electromagnetic action that avoids this weak equivalence principle constraint.
[63]D. Graham, P. Nelson, and R. Newman, in *Tests of Fundamental Laws in Physics* (Ref. 30), p. 459.
[64]R. Cowsik, N. Krishnan, S.N. Tandon, and S. Unnikrishnan, Phys. Rev. Lett. **64**, 336 (1990).

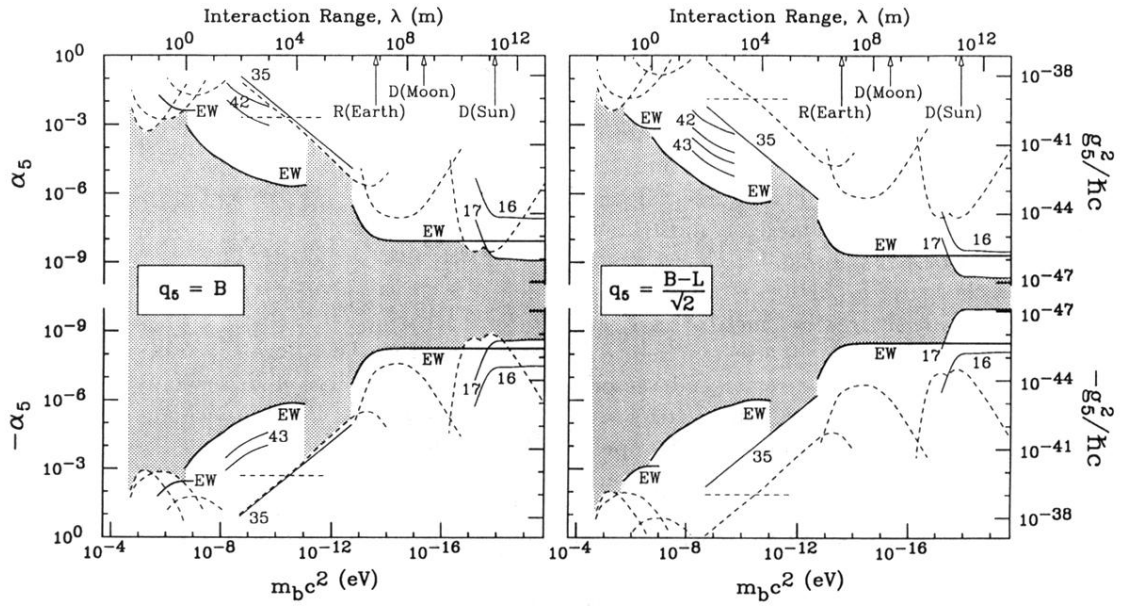

FIG. 25. 2σ constraints on interactions of ultra-low-mass vector bosons from this and previous experiments. Upper limits on α_5, or g_5^2, as a function of boson mass $m_b c^2$, or range λ. Although one expects α_5 to have a positive sign corresponding to the repulsive vector interaction between like charges, for simplicity in interpreting experimental results which can have either sign we consider the possibility of negative α_5 as well. Dashed curves are from tests of the $1/r^2$ law. The horizontal dashed constraints are from Ref. 40; the remaining dashed curves from work summarized in Ref. 39. Solid curves are from composition dependence experiments; numbers on the curves correspond to references in the text. Left panel: $q_5 = B$; right panel: $q_5 \propto B - L$. The curves labeled EW are from this work.

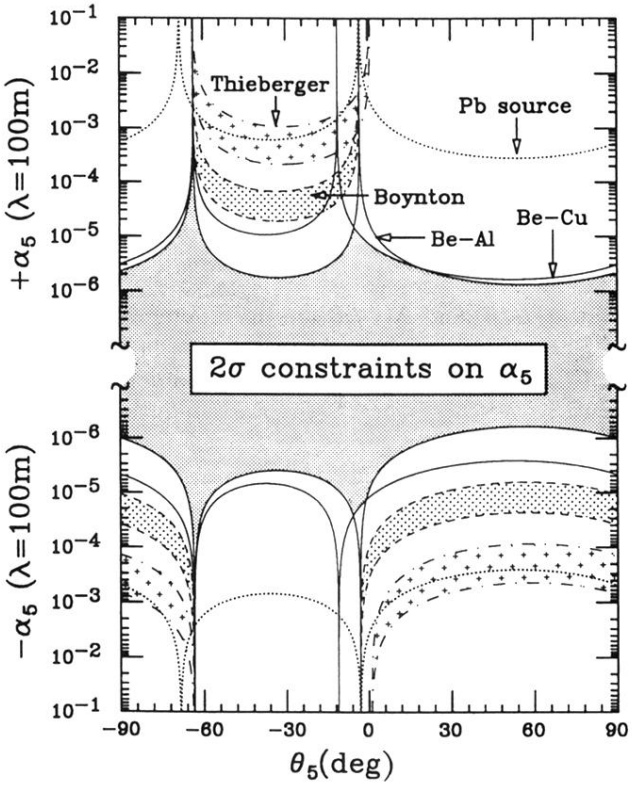

FIG. 26. Constraints on α_5 as a function of mixing angle θ_5 for a vector interaction with an assumed range λ=100 m. The dotted curve labeled *Pb source* is from our laboratory source experiment described below. The heavily shaded region is allowed by our results. For comparison, we show constraints corresponding to the positive results reported by Thieberger (Ref. 43) and Boynton *et al.* (Ref. 44).

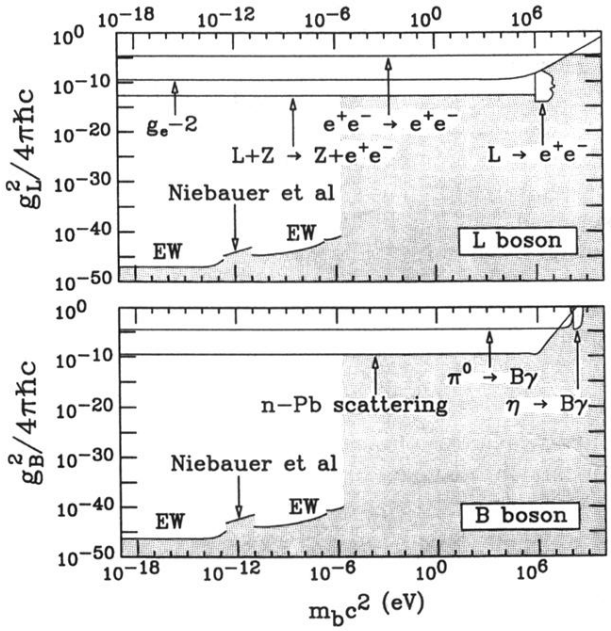

FIG. 27. 2σ constraints on the couplings of proposed L and B bosons coupled to L and B, respectively. The vertical axes display coupling strengths defined in Eq. (1). The curves labeled EW are from this work.

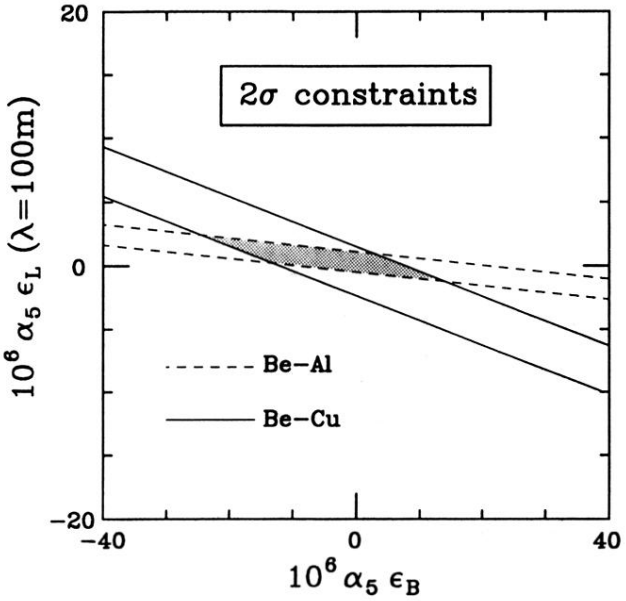

FIG. 29. Constraints on interactions of ultra-low-mass scalar bosons from this experiment.

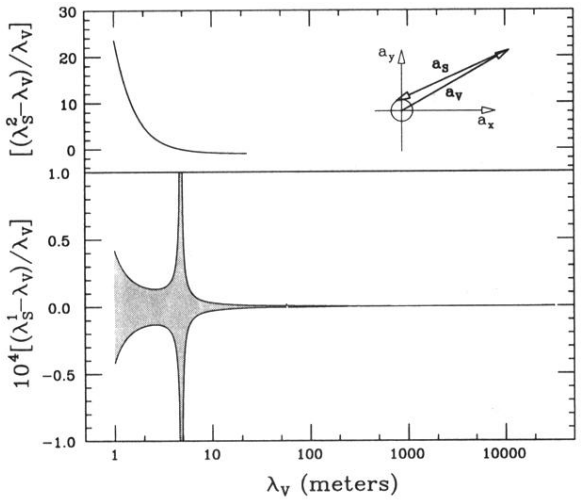

FIG. 30. Constraints from our Be/Cu data on parameters of a proposed "quantum gravity" model in which the gravivector interaction couples to B with α_V=1. The allowed difference $\Delta\lambda = \lambda_S - \lambda_V$ is shown as a function of λ_V. Because our source integrals (see Fig. 24) have a maximum at $\lambda \approx 5$ m, there are two solutions denoted by λ_S^1 and λ_S^2. The 1σ regions consistent with our data are shaded. Top panel: solution 1; the allowed region is much smaller than the width of the line. The inset shows how the gravivector and graviscalar accelerations must lie within our error circle. Bottom panel: solution 2. Within either allowed region the constraints are satisfied only for a very narrow range of α_S/α_V. For example, at $\lambda_V = 10$ km, the product $\alpha_S\Delta(q_S/\mu)_{\rm det}\,(q_S/\mu)_{\rm source}I_S$ must lie within ≈ 1 part in 10^6 of the corresponding vector quantity.

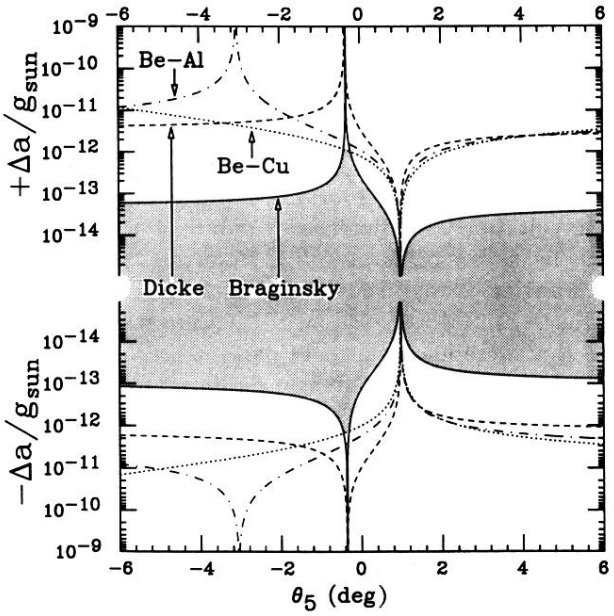

FIG. 31. Maximum contribution of a $\lambda = \infty$ vector interaction to the Earth-Moon differential acceleration toward the Sun, showing 2σ constraints from our Be/Cu and Be/Al data, and the RKD and Braginsky-Panov solar Eötvös experiments. The zero occurs because the earth-moon charge difference vanishes at $\theta_5 \approx 1°$. The poles occur at values of θ_5 where the charge difference vanishes for the Al/Au and Al/Pt test body pairs used in the RKD and Braginsky-Panov experiments. Outside the range of this plot, the upper limits on $\Delta a/a$ from the solar experiments are essentially independent of θ_5; the Eöt-Wash constraint has a zero at $\theta_5 \approx -49°$ where the charge of the Sun vanishes. The joint constraints for any value of θ_5 are thus at least as stringent as those shown on this plot. Note that the gravitational binding energy of the Earth is 5.1×10^{-10} of its mass.

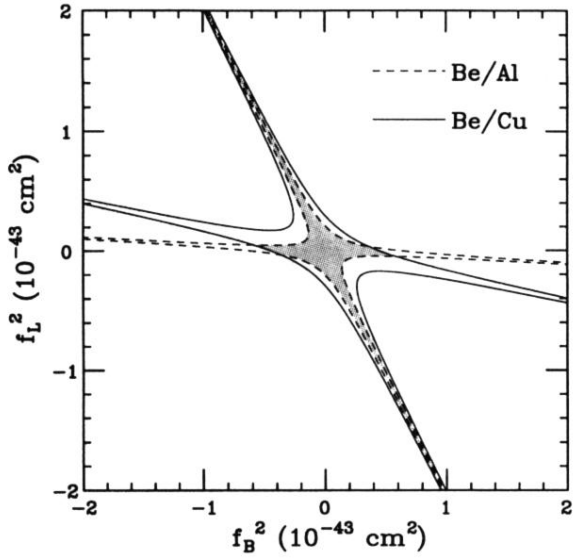

FIG. 32. 1 σ constraints on the parameters f_B^2 and f_L^2 of Moffat's nonsymmetric theory of gravity as analyzed by Will.

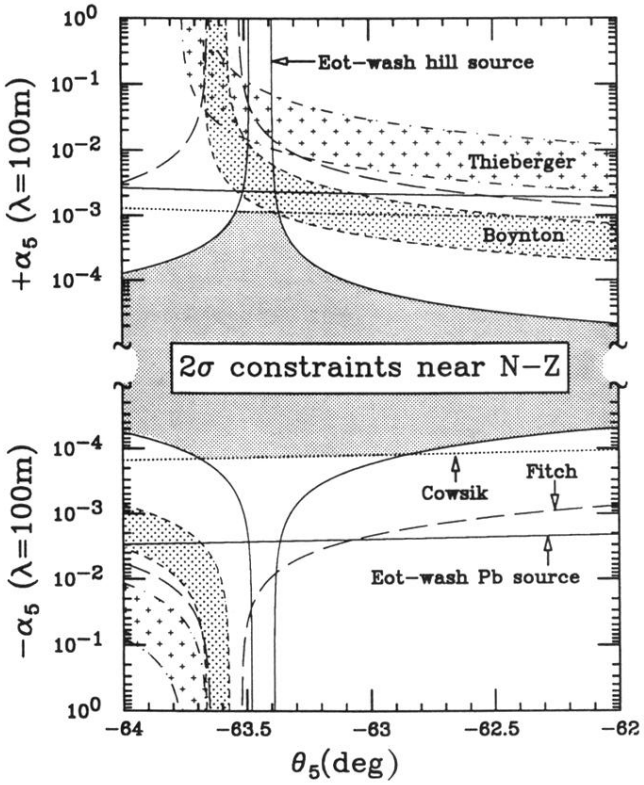

FIG. 35. Constraints on vector interactions coupled predominantly to $B - 2L$ from this and other work. This plot enlarges the region around $\theta_5 = -63°$ shown in Fig. 26. The heavily shaded region is allowed by our work and that of Ref. 63. Uncertainties in the chemical compositions of the different sources were taken from Refs. 44 and 46. This analysis supersedes that in Ref. 18.